51st AIAA Aerospace Sciences Meeting including the New Horizons Forum and Aerospace Exposition
07 - 10 January 2013, Grapevine (Dallas/Ft. Worth Region), Texas

AIAA 2013-0522

Numerical Simulation of Graphite Ablation Induced Outgassing Effects on Hypersonic Boundary Layer Receptivity over a Cone Frustum

Clifton H. Mortensen* and Xiaolin Zhong†
University of California, Los Angeles, California, 90095, USA

A new thermochemical nonequilibrium linear stability theory code with a gas phase model including multiple carbon species is developed and validated. A high-order shock-fitting method with thermochemical nonequilibrium and surface chemistry boundary conditions for graphite ablation along with the new linear stability theory code are used to study hypersonic boundary layer receptivity and stability for a 7° half angle blunt cone at Mach 15.99. The real gas results are compared with ideal gas computations that set their wall temperature and wall blowing from the real gas simulation. Weak planar fast acoustic waves are used to perturb the steady base flow. A 525 kHz disturbance was found to be unstable for the real gas simulation and stable for both ideal gas simulations. The second mode for the 525 kHz disturbance becomes the dominant instability mode on the cone frustum for the thermochemical nonequilibrium simulation.

Nomenclature

$\dot{m}'$	Mass flux per area $kg/m^2 \cdot s$
c_r	Phase speed m/s
C_s	Mass fraction of species s
$c_{v,s}$	Species translation-rotation heat capacity at constant volume J/kgK
e	Specific total energy J/kg
$e_{v,s}$	Species specific vibration energy J/kg
e_v	Specific vibration energy J/kg
F	Inviscid flux vector
G	Viscous flux vector
h_o	Stagnation enthalpy J/kg
h_s^o	Species heat of formation J/kg
M_s	Species molecular weight kg/mol
nms	Number of molecular species
ns	Number of species
$Q_{T-V,s}$	Species vibration energy transfer rate J/s
R	Universal gas constant 8.3143 $J/mol \cdot K$
s	Surface streamline
T	Translation-rotation temperature K
T_V	Vibration temperature K
U	Vector of conserved flow variables
v_w	Wall normal velocity m/s
W	Source vector
X_s	Molar concentration of species s mol/m^3

Subscripts

∞	Freestream
n	Wall normal
s	Species
t	Wall tangent
w	Wall

Symbols

α_r	Wavenumber $1/m$
$-\alpha_i$	Growth rate $1/m$
ΔZ	Perturbation amplitude of Z
ΔZ_r	Real part of Z perturbation
δ_{ij}	Kronecker delta
μ	Viscosity $kg/s \cdot m$
ω_s	Rate of species production $kg/m^3 \cdot s$
ρ	Density kg/m^3
σ	Stefan-Boltzmann constant

*Graduate Student, Mechanical and Aerospace Engineering, cmort22@gmail.com, AIAA Student Member.
†Professor, Mechanical and Aerospace Engineering, xiaolin@seas.ucla.edu, AIAA Associate Fellow.

I. Introduction

Thermal protection systems (TPS) are commonly used to protect hypersonic vehicles from the harsh high enthalpy environment they operate in.[1] Often a TPS is ablating such as those made using graphite or phenolic impregnated carbon ablator. Examples include nose cones or fins for thermal protection of hypersonic missiles and more recently SpaceX's Dragon capsule's heat shield. The design of these thermal protection systems is of major concern to the vehicle designer who must ensure the structural integrity of the vehicle throughout its flight envelope. Experimental testing of the various designs can be done in the laboratory or by flight tests. However the ground based simulation of the exact hypersonic flow conditions encountered in free flight may not be possible and free flight data does not yield the behavior of the entire flow field. Thus, numerical simulations play an important role as a complement to laboratory and flight test research as free flight conditions can be replicated and the entire flow field can be resolved.

A major consideration when evaluating the effectiveness of a TPS is estimation of boundary layer transition which has a strong effect on surface heating rates. A turbulent boundary layer has a much higher heating rate than a corresponding laminar boundary layer. If boundary layer transition can be estimated accurately it can help the thermal protection designer minimize its safety factor and thus the vehicle weight. It is commonly understood that for flat plates and straight cones in a low disturbance environment the amplification of linear wave like disturbances such as the second mode for hypersonic flows can lead to parametric instabilities and mode interactions and then to breakdown and finally turbulence. Eigenmode growth of linear wavelike disturbances is generally the slowest part of the transition process and the most unstable frequencies persist downstream. This makes the eigenmode growth region essential to understanding hypersonic boundary layer transition. Common methods for modeling these linear wave like disturbances are linear stability theory (LST), parabolized stability equations (PSE) and direct numerical simulation (DNS). These methods are designed to predict the growth or decay of wave like disturbances based on a laminar mean flow profile. This research will focus on using LST and DNS to study the real gas effects of ablation induced outgassing on hypersonic boundary layer stability over a cone frustum.

Significant research on the linear stability of boundary layers has been performed by Mack.[2] Mack found that the major instability waves for hypersonic boundary layers with a perfect gas assumption are the first and second modes. Following researchers have implemented numerical codes using linear stability theory to compute the most unstable frequencies for a variety of flow conditions and gas models. Malik[3] implemented multiple numerical methods for linear stability of perfect gas boundary layer flows. Most research on hypersonic boundary layer stability has used a perfect gas model and few researchers have studied effects of thermochemical nonequilibrium. Chang et al.[4] comment on real gas effects stating that it is "very important to account for the chemistry effect in future transition for hypersonic vehicles." Stuckert and Reed,[5] Hudson et al.,[6,7] Chang et al.[4] and Johnson et al.[8] studied boundary layer stability in nonequilibrium chemically reacting hypersonic boundary layers using linear stability theory. It was found that dissociation of air species is destabilizing to the second mode and stabilizing to the first mode. Ma and Zhong[9] studied the receptivity of free stream disturbances using DNS for a Mach 10 nonequilibrium oxygen flow over a flat plate. They found that in a Mach 10 oxygen flow there is a significant real gas destabilizing effect on the second-mode waves. However they did not consider thermal nonequilibrium or any gas/surface interaction. Prakash et al.[10] studied receptivity of freestream disturbances with a thermochemical nonequilibrium shock-fitting method. Parsons et al.[11] studied the receptivity effects of thermochemical nonequilibrium on blunt cones. They found that freestream acoustic waves had higher pressure perturbation amplitudes for a flow with thermochemical nonequilibrium than a perfect gas. Also they found that the maximum perturbation amplitude moved nearer to the blunt nose.

Currently there has been a limited amount of numerical research on how ablation and surface chemistry models effect hypersonic boundary layer receptivity and stability. Johnson et al.[12] used linear stability analysis to analyze non-reacting and reacting hypersonic boundary layer stability with blowing and suction. Ghaffari et al.[13] performed a linear stability analysis of a hypersonic perfect gas flat plate boundary layer with wall blowing and found that as blowing increases the maximum amplification rate of the disturbance instability grows and moves to lower frequencies. Li et al.[14] studied boundary layer instability mechanisms for hypersonic perfect gas flows over slender cones and blunt capsules at zero angle of attack and an angle of attack of 16°. They found that for the slender cone out-gassing is moderately stabilizing to the second mode and for the blunt capsule out-gassing is destabilizing to the first mode. Mortensen and Zhong[15] performed an initial DNS study of a M_∞=15.99 blunt cone with surface chemistry boundary conditions showing that real gas velocity perturbations at the wall grew an order of magnitude larger than perfect gas perturbations.

The goal of this paper is twofold: 1) to validate a new thermochemical nonequilibrium linear stability theory code where the gas species model those encountered from graphite ablation and 2) to study the real gas effects of graphite ablation induced outgassing on hypersonic boundary layer stability over a cone frustum. A thermochemical nonequilibrium linear stability theory code is required to help analyze boundary layer waves such as identifying the fast and slow acoustic waves. A new LST code needed to be written because the source code was required to add in the carbon species due to ablation and to add a linearized version of the surface chemistry model. An eleven species gas model is used to model chemical nonequilibrium. It contains a standard five species air model (N_2, O_2, NO, N, O). The remaining species contain carbon (C_3, CO_2, C_2, CO, CN, C) and are obtained from sublimation, oxidation and ablation product reactions. A two-temperature model is used to simulate thermal nonequilibrium. Only graphite ablation is considered without the effects of charring, pyrolysis, surface recession and ablation induced roughness. The surface reactions considered contain oxidation, recombination of atomic oxygen and sublimation. A surface mass balance is used to set species mass fractions at the surface and temperature profiles within the ablator are not computed. A simplified approach to ablation prediction is used to help keep the research focus on hypersonic boundary layer receptivity and stability.

The paper will start with an overview of the governing equations and the gas phase models followed by the numerical methods for both the DNS and LST codes. An overview of the surface chemistry model as well as the required boundary conditions for both methods are then given. After which the LST code will be validated with unsteady data computed from the DNS code which was previously validated by Mortensen and Zhong.[15] After validation, a simulation of a 7° half angle blunt cone at Mach 15.99 is performed to study hypersonic boundary layer receptivity and stability with thermochemical nonequilibrium and graphite ablation over a cone frustum.

II. Governing Equations and Gas Phase Models

The governing equations for thermochemical nonequilibrium are formulated for a two-temperature model with the rotational energy mode assumed to be fully excited and eleven non-ionizing species with finite rate chemistry. Two temperatures are used to represent translation-rotation energy and vibration energy. The eleven species model (N_2, O_2, NO, C_3, CO_2, C_2, CO, CN, N, O, C) is used to simulate air, surface reactions, and reactions of air with ablation products. The conservative three-dimensional Navier-Stokes equations consist of eleven species mass conservation equations, three momentum conservation equations, the vibration energy conservation equation and the total energy conservation equation. Wang and Zhong,[16] Prakash et al.[17] and Mortensen and Zhong[15] have used similar formulations for shock-fitting DNS of thermochemical nonequilibrium flow. For both LST and DNS the governing equations as well as the gas phase models are the same. Written in vector form the governing equations are

$$\frac{\partial U}{\partial t} + \frac{\partial F_j}{\partial x_j} + \frac{\partial G_j}{\partial x_j} = W \tag{1}$$

where U is the state vector of conserved quantities and W is the source terms defined by

$$U = \begin{bmatrix} \rho_1 \\ \vdots \\ \rho_{ns} \\ \rho u_1 \\ \rho u_2 \\ \rho u_3 \\ \rho e \\ \rho e_v \end{bmatrix}, \quad W = \begin{bmatrix} \omega_1 \\ \vdots \\ \omega_{ns} \\ 0 \\ 0 \\ 0 \\ 0 \\ \sum_{s=1}^{nms} (Q_{T-V,s} + \omega_s e_{v,s}) \end{bmatrix}.$$

F_j and G_j are the inviscid and viscous fluxes respectively and are defined by

$$F_j = \begin{bmatrix} \rho_1 u_j \\ \vdots \\ \rho_{ns} u_j \\ \rho u_1 u_j + p\delta_{1j} \\ \rho u_2 u_j + p\delta_{2j} \\ \rho u_3 u_j + p\delta_{3j} \\ (\rho e + p)\, u_j \\ \rho e_v u_j \end{bmatrix}, \quad G_j = \begin{bmatrix} \rho_1 v_{1j} \\ \vdots \\ \rho_{ns} v_{nsj} \\ \tau_{1j} \\ \tau_{2j} \\ \tau_{3j} \\ -u_i \tau_{ij} - k_T \frac{\partial T}{\partial x_j} - k_V \frac{\partial T_V}{\partial x_j} + \sum_{s=1}^{nms} \rho_s h_s v_{sj} \\ -k_V \frac{\partial T_V}{\partial x_j} + \sum_{s=1}^{nms} \rho_s e_{v,s} v_{sj} \end{bmatrix}$$

where $v_{sj} = u_{sj} - u_j$ is the species diffusion velocity and $\tau_{ij} = \mu\left(\frac{\partial u_i}{\partial x_j} + \frac{\partial u_j}{\partial x_i}\right) - \frac{2}{3}\mu\frac{\partial u_k}{\partial x_k}\delta_{ij}$ is the viscous stress. The total energy per unit volume, ρe, is defined by

$$\rho e = \sum_{s=1}^{ns} \rho_s c_{v,s} T + \rho e_v + \frac{1}{2}\rho u_i u_i + \sum_{s=1}^{ns} \rho_s h_s^{\circ} \tag{2}$$

where h_s° is the heat of formation of species s and $c_{v,s}$ is the species translation-rotation specific heat at constant volume defined as

$$c_{v,s} = \begin{cases} \frac{5}{2}\frac{R}{M_s}, & s = 1, 2, \ldots, nms \\ \frac{3}{2}\frac{R}{M_s}, & s = nms+1, \ldots, ns. \end{cases} \tag{3}$$

The vibration energy per unit volume, ρe_v, is defined as

$$\rho e_v = \sum_{s=1}^{nms} \rho_s e_{v,s} = \sum_{s=1}^{nms} \rho_s \left(\sum_{m=1}^{nmod} \frac{g_{s,m} R}{M_s} \frac{\theta_{v,s,m}}{\exp\left(\theta_{v,s,m}/T_V\right) - 1} \right) \tag{4}$$

where *nmod* refers to the number of vibrational modes for each polyatomic molecule, $\theta_{v,s,m}$ refers to the characteristic temperature of each vibrational mode, and $g_{s,m}$ is the degeneracy of each vibrational mode. For the diatomic species there is only one vibrational mode and the degeneracy is unity. For C_3 and CO_2 there are three vibrational modes where two modes have a degeneracy of unity and one has a degeneracy of two. The characteristic vibration temperatures and their degeneracies were taken from Park[18] for N_2, O_2 and NO, from Dolton et al.[19] for C_3, and from McBride[20] for CO_2, C_2, CO, and CN.

To model chemical nonequilibrium eight dissociation reactions and sixteen exchange reactions are used. Each reaction is governed by a forward and backward reaction rate determined by Eqs. (5) and (6) respectively. The forward reaction rates and constants are obtained Park,[21] Bhutta & Lewis[22] and Park et al.[23] The equilibrium coefficient, K_{eq}, is computed in two different ways. The first is a curve fit from Park[18] as in Eq. (7). The second is from the Gibbs Free energy approach where curve fits to the Gibbs Free energy are obtained from McBride et al.[20] as in Eqs. (8) and (9) respectively.

$$k_f = C_f T_a^{\eta} e^{(-\theta_d/T_a)} \tag{5}$$

$$k_b = k_f / K_{eq} \tag{6}$$

$$K_{eq} = A_0 \exp\left(\frac{A_1}{Z} + A_2 + A_3 \ln(Z) + A_4 Z + A_5 Z^2\right), \quad Z = \frac{10000}{T} \tag{7}$$

$$\frac{G^{\circ}}{RT} = a_1(1 - \ln T) - \frac{a_2}{2}T - \frac{a_3}{6}T^2 - \frac{a_4}{12}T^3 - \frac{a_5}{20}T^4 + \frac{a_6}{T} - a_7 \tag{8}$$

$$K_{eq} = \exp\left(-\frac{G^{\circ}}{RT}\right)(R_u T)^{-\Delta n} \tag{9}$$

To calculate the source term in the vibration energy equation representing the exchange of energy between the translation-rotation and vibration energies the Landau-Teller formulation is used

$$Q_{T-V,s} = \rho_s \frac{e_{v,s}(T) - e_{v,s}(T_V)}{< \tau_s > + \tau_{cs}} \tag{10}$$

where $< \tau_s >$ is the Landau-Teller vibration relaxation time given by Lee.[24] τ_{cs} is from Park[18] to more accurately model the relaxation time in areas of high temperatures occurring just downstream of the bow schock.

The viscosity of each species is computed using a Blottner curve fit shown in Eq. (11). The coefficients are obtained from Blottner,[25] Gupta,[26] and Candler.[27] The mixture viscosity is then found using each species viscosity from a mixing rule obtained from Wilke[28] (Eq. (12)). The total heat conductivities for each energy mode are computed in a similar fashion as viscosity. The diffusion velocity is calculated using Fick's law and a constant Schmidt number of 0.5.

$$\mu_s = 0.1 \exp\left[\left(A_s^\mu \ln\left(T\right) + B_s^\mu\right) \ln\left(T\right) + C_s^\mu\right] \tag{11}$$

$$\mu = \sum_{s=1}^{ns} \frac{X_s \mu_s}{\phi_s} \tag{12}$$

III. Numerical Method

A. DNS Numerical Method

A high-order shock-fitting method developed for perfect gas flow by Zhong[29] has been extended for use on thermochemical nonequilibrium flows to compute the flow field between the shock and the body. For shock-fitting computations the shock location is not known *a priori* so its position is solved along with the flow field. Since the shock position is not stationary the grid used to compute the flow field is a function of time. This leads to the coordinate transformation

$$\begin{cases} \xi = \xi(x,y,z) \\ \eta = \eta(x,y,z,t) \\ \zeta = \zeta(x,y,z) \\ \tau = t \end{cases} \Longleftrightarrow \begin{cases} x = x(\xi,\eta,\zeta,\tau) \\ y = y(\xi,\eta,\zeta,\tau) \\ z = z(\xi,\eta,\zeta,\tau) \\ t = \tau \end{cases}$$

where y is normal to the body, x is in the streamwise direction, z is in the transverse direction, $\zeta_t = 0$ and $\xi_t = 0$. The governing equation can then be transformed into computational space as

$$\frac{1}{J}\frac{\partial U}{\partial \tau} + \frac{\partial E'}{\partial \xi} + \frac{\partial F'}{\partial \eta} + \frac{\partial G'}{\partial \zeta} + \frac{\partial E'_v}{\partial \xi} + \frac{\partial F'_v}{\partial \eta} + \frac{\partial G'_v}{\partial \zeta} + U\frac{\partial (1/J)}{\partial \tau} = \frac{W}{J} \tag{13}$$

where J is the Jacobian of the coordinate transformation and

$$E' = \frac{F_1\xi_x + F_2\xi_y + F_3\xi_z}{J} \tag{14}$$

$$F' = \frac{F_1\eta_x + F_2\eta_y + F_3\eta_z}{J} \tag{15}$$

$$G' = \frac{F_1\zeta_x + F_2\zeta_y + F_3\zeta_z}{J} \tag{16}$$

$$E'_v = \frac{G_1\xi_x + G_2\xi_y + G_3\xi_z}{J} \tag{17}$$

$$F'_v = \frac{G_1\eta_x + G_2\eta_y + G_3\eta_z}{J} \tag{18}$$

$$G'_v = \frac{G_1\zeta_x + G_2\zeta_y + G_3\zeta_z}{J}. \tag{19}$$

A seven point stencil is used to discretize the spatial derivatives

$$\frac{df_i}{dx} = \frac{1}{hb_i}\sum_{k=-3}^{3} \alpha_{i+k} f_{i+k} - \frac{\alpha}{6!b_i} h^5 \left(\frac{\partial f^6}{\partial^6 x}\right) \tag{20}$$

where

$$a_{i\pm3} = \pm 1 + \frac{1}{12}\alpha, \qquad a_{i\pm2} = \mp 9 - \frac{1}{2}\alpha \tag{21}$$

$$a_{i\pm1} = \pm 45 + \frac{5}{4}\alpha, \qquad a_i = -\frac{5}{3}\alpha \tag{22}$$

$$b_i = 60 \tag{23}$$

and where $\alpha < 0$ is a fifth order upwind explicit scheme and $\alpha = 0$ reduces to a sixth order central scheme. Here the inviscid terms use $\alpha = -6$ which yields a low dissipation fifth order upwinded difference and the viscous terms are discretized using $\alpha = 0$. Flux splitting is used for the inviscid flux terms and to compute second derivatives the first order derivative operator is applied twice.

Conditions behind the shock are calculated from Rankine-Hugoniot relations. In the freestream the flow is assumed to be in thermal equilibrium and the chemical composition of the flow is frozen. The shock is assumed to be infinitely thin which means that the flow has no time to relax as it crosses the shock as relaxation rates are finite. This leads to the chemical composition remaining constant across the shock as well as the vibration temperature. Since neither process has any time to relax across the shock the relaxation zone is entirely downstream of the shock. A complete derivation of thermochemical nonequilibrium shock fitting can be found from Prakash et al.[10] Explicit Euler is used to advance the solution in time.

B. LST Numerical Method

The derivation of the thermochemical nonequilibrium LST equations follows the work of Hudson.[7] The main difference in the derivation is that here the equation for each species velocity is substituted into the governing equations before they are linearized similar to Klentzman et al.[30] The LST equations are derived from the governing equations (Eq. (1)) where the instantaneous flow is comprised of a mean and fluctuating component $q = \bar{q} + q'$. Here q represents any flow variable such as velocity, density, temperature, &c. The instantaneous flow is then substituted into the governing equations where the steady flow is assumed to satisfy the governing equations and is subtracted out. The mean flow is assumed to be a function of y only i.e. $\bar{q}(x, y, z) = \bar{q}(y)$ and the flow disturbances are assumed to be small i.e. linear. The perturbations are then assumed to be in the form of a normal mode described by

$$q'(x, y, z) = \hat{q}(y) \exp\left[i\left(\alpha x + \beta z - \omega t\right)\right] \tag{24}$$

where ω is the circular frequency of the disturbance and α and β are the wavenumbers. Commonly ω and β are assumed to be real and the wavenumber α is assumed to be complex which means the disturbances grow in space rather than time. If α is complex and ω and β are real then the disturbances grow in time rather than space. For comparison to direct numerical simulation the spatial stability approach is used i.e. α is complex which results in the dispersion relation $\alpha = \Omega(\omega, \beta)$. Substituting in the normal mode form for the perturbation reduces the problem to a coupled set of ns+5 ordinary differential equations

$$\left(\mathbf{A}\frac{d^2}{dy^2} + \mathbf{B}\frac{d}{dy} + \mathbf{C}\right)\vec{\phi} = \vec{0} \tag{25}$$

where $\vec{\phi} = \{\hat{\rho}_1, \hat{\rho}_2, ..., \hat{\rho}_{ns}, \hat{u}, \hat{v}, \hat{w}, \hat{T}, \hat{T}_V\}^T$ and $\mathbf{A}$, $\mathbf{B}$ and $\mathbf{C}$ are complex square matrices of size ns+5. This is now a boundary value problem where the derivative operators can be discretized and the equations solved numerically.

For hypersonic compressible boundary layers it is important to have high grid resolution near the generalized inflection point.[2] The current computational grid is used to cluster grid points around the inflection point and has been used by previous researchers.[6] It is defined so

$$y = \frac{a\eta}{b - \eta} \tag{26}$$

where

$$a = \frac{y_{max} y_i}{(y_{max} - 2y_i)} \tag{27}$$

$$b = 1 + \frac{a}{y_{max}} \tag{28}$$

and y_{max} is the outer domain boundary, y_i is the location of the generalized inflection point and η runs from zero to one. For a cone frustum a generalized inflection point may not exist so y_i is placed near the boundary layer edge. Grid metrics can be computed directly from Eq. (26).

With the grid defined, Eq. (25) can be transformed into computational space and a numerical representation of the derivatives given. The derivatives are approximated using a fourth order central difference scheme which yields

$$\frac{\partial \phi}{\partial \eta} = \frac{-\phi_{i+2} + 8\phi_{i+1} - 8\phi_{i-1} + \phi_{i-2}}{12\Delta\eta} \tag{29}$$

$$\frac{\partial^2 \phi}{\partial \eta^2} = \frac{-\phi_{i+2} + 16\phi_{i+1} - 30\phi_j + 16\phi_{i-1} - \phi_{i-2}}{12\Delta\eta^2}. \tag{30}$$

This high order central difference scheme has been used by previous researchers[7,31] to good effect. It is also possible to discretize the derivatives using a multi domain spectral collocation approach to achieve a high order of accuracy.[3] It may be beneficial to implement a high order spectral method when many species are required to cut the computational cost as the number of equations to solve in Eq. (25) increases linearly with the number of species.

After discretization, nonlinearities exist in α so the global method suggested by Malik[3] is used to compute the eigenvalue spectrum with $\alpha^2 = 0$. This method computes the eigenvalues from a generalized eigenvalue problem $\tilde{A}\vec{\phi} = \alpha\tilde{B}\vec{\phi}$ where the LAPACK[32] subroutine ZGGEV is used here for solution. From the eigenvalue spectrum an initial guess can be obtained for the local method which results in $\bar{A}\phi = \bar{B}$ and the eigenvalue is found iteratively without dropping the α^2 terms. The LAPACK subroutine ZGESV is used to solve the local problem. It is also possible to avoid the computationally intensive global method and obtain an initial guess for α from a nearby streamwise location or a DNS simulation *assuming* the unsteady DNS results are available.

IV. Surface Chemistry Model and Boundary Conditions

For the two stability methods different boundary conditions are required. DNS boundary conditions are required at the wall, outlet, symmetry plane and shock. The surface chemistry model is applied at the wall for the DNS simulation but has not been linearized yet to be used by the LST code. For LST boundary conditions are required at the wall and outside the boundary layer or at the shock. Here LST boundary conditions are applied outside the boundary layer instead of at the shock.

A. DNS Surface Chemistry Model

The surface chemistry model contains oxidation, recombination of atomic oxygen and sublimation of C, C_2 and C_3. Six surface reactions are taken into account. The first two reactions allow for surface removal of material through oxidation and the third equation gives the recombination of atomic oxygen. The reactions and reaction probabilities for oxidation and recombination of atomic oxygen are obtained from Park.[33] The reaction probabilities for all three sublimation products were obtained experimentally by Palmer.[34] C_3 is included in most graphite ablation models because sublimation of graphite produces mostly C_3 with smaller amounts of C, C_2 and heavier carbon species.

$$(C) + O_2 \rightarrow CO + O \tag{31}$$

$$(C) + O \rightarrow CO \tag{32}$$

$$(C) + O + O \rightarrow (C) + O_2 \tag{33}$$

The oxidation rates are based on kinetic theory giving

$$k_{w,r} = \alpha_{rp}\sqrt{\frac{RT_w}{2\pi M_s}} \tag{34}$$

where α_{rp} is the reaction probability for each reaction obtained experimentally to be

$$\alpha_1 = \frac{1.43 \times 10^{-3} + 0.01 \exp\left(-1450/T_w\right)}{1 + 2 \times 10^{-4} \exp\left(13000/T_w\right)} \tag{35}$$

$$\alpha_2 = 0.63 \exp\left(-1160/T_w\right) \tag{36}$$

$$\alpha_3 = 0.63 \exp\left(-1160/T_w\right). \tag{37}$$

There are three reactions for sublimation

$$(C) \rightarrow C \tag{38}$$

$$(C) \rightarrow C_2 \tag{39}$$

$$(C) \rightarrow C_3 \tag{40}$$

and for each reaction the mass flux is obtained from the Knudsen-Langmuir equation[35]

$$\dot{m}'_s = \alpha_s \left(p_{v,s} - p_s\right) \sqrt{\frac{M_s}{2\pi R T_w}} \tag{41}$$

where α_s is experimentally determined for each carbon species. The vapor pressure of the three carbon species is given by

$$p_{v,s} = \exp\left(\frac{P_s}{T_w} + Q_s\right) \quad p \text{ in } atm \tag{42}$$

where Table 1 gives the reaction probabilities and vapor pressure coefficients for each sublimation reaction.

Table 1. Sublimation reaction probabilities and vapor pressure coefficients.

	α_s	P_s	Q_s
C	0.14	-85715	18.69
C_2	0.26	-98363	22.20
C_3	0.03	-93227	23.93

* α_s from Palmer[34] and P_s and Q_s from.[19]

Boundary conditions are needed to couple the surface chemistry model with the gas model as well as set wall conditions for temperature and pressure. At the wall a surface energy balance needs to be solved to find temperature and a surface mass balance needs to be solved to find the mass fraction for each species. A simplified surface energy balance is used to avoid a complicated flow/solid coupling and allowing the focus of the simulation to stay on boundary layer stability. The surface energy balance is

$$k_T \frac{\partial T}{\partial n} + k_V \frac{\partial T_V}{\partial n} + \sum_{s=1}^{ns} \rho h_s D_s \frac{\partial C_s}{\partial n} = \sigma \epsilon T_w^4 + \dot{m}'_w \sum_{s=1}^{ns} C_s h_{s,o} \tag{43}$$

where

$$h_{s,o} = \left(c_{v,s} + \frac{R}{M_s}\right) T + e_{v,s} + h_s^o + \frac{1}{2}\left(u_1^2 + u_2^2 + u_3^2\right) \tag{44}$$

and all values and derivatives are taken at the wall. $\epsilon = 0.9$ for the carbon surface and σ is the Stefan-Boltzmann constant. Each derivative is taken normal to the surface where n represents the direction normal to the surface. High order Lagrange polynomials are used to compute the normal derivatives at the surface. The surface mass balance for each species is

$$\rho_{s,w} v_w - \rho_w D_w \frac{\partial C_{s,w}}{\partial n} = \dot{m}'_s. \tag{45}$$

The total mass balance found from summing Eq. (45) is

$$\rho_w v_w = \dot{m}'_w \tag{46}$$

where the total mass flux is found from the sum of each species mass flux as

$$\dot{m}'_w = \sum_{s=1}^{ns} \dot{m}'_s. \tag{47}$$

The last required condition at the surface is for pressure. High order pressure extrapolation using Lagrange polynomials is used to set the surface pressure.

B. LST Boundary Conditions

The boundary conditions for Eq. (25) are the linearized non-catalytic wall conditions for density, no slip, zero temperature perturbation at the wall and all perturbation conditions are zero in the freestream except wall normal velocity. The freestream wall normal velocity perturbation is found using the mass conservation equation similar to Hudson.[6] For an optimal comparison of LST to DNS the linearized surface chemistry boundary conditions need to be used. Work is currently underway to linearize the surface chemistry boundary conditions but it is not complete yet.

V. LST Validation

To validate the new LST code a comparison is performed between the results of the LST code and results from a DNS simulation. In the DNS simulation the entire flow field is computed with a disturbance imposed in the freestream which differs from LST where only a single wall normal slice is required and no disturbance is introduced. Some of the simplifying assumptions made in the derivation of the LST equations are not made in DNS such as the parallel flow assumption but both methods for this case do assume that disturbances are linear. The main difference between the two methods is that the boundary conditions are different. For the DNS code the surface chemistry model is used at the wall and for the LST code it is not. Also, there are perturbations outside the boundary layer for the DNS simulation where LST assumes that all the perturbations are zero at a specified location outside the boundary layer except wall normal velocity. Despite these differences an accurate comparison for the mode shape, wavenumber and growth rate can be obtained. Achieving an accurate comparison between the stability results of these two different stability methods will lend credibility to the proper implementation of both methods.

Before a code comparison can be performed a grid convergence study must be done to determine the required number of grid points for the LST grid. Three different grid densities were used with 100, 200 and 300 points respectively. A comparison for the amplification rate at multiple frequencies as well as the temperature perturbation amplitude for a 525 kHz disturbance is given in Figure 1. For the 200 grid point solution the percent relative error for the amplification rate is less than one percent for the majority of the unstable frequency range. The error increases near the edges of the frequency range because the amplification rate is near zero. There are only slight changes in the temperature perturbation amplitude between all three solutions. Two hundred grid points yields a grid converged solution for this streamwise location.

In the DNS simulation fast acoustic waves in the freestream are imposed on the bow shock and then their behavior is simulated as they pass through the entire domain. This approach does not simulate the behavior of a single mode like LST but rather multiple modes can be present for each frequency. For the most consistent comparison a streamwise location was selected where DNS results showed a constant exponential disturbance growth. This was done because constant exponential growth is indicative of modal growth and therefore a dominant boundary layer mode rather than multiple competing modes. The streamwise location selected is located at s=0.564 m downstream measured along the cone surface from the stagnation point.

Figure 2 shows the steady boundary layer profile computed by DNS. Here u and v represent the velocity components parallel to the wall and normal to the wall respectively. Significant thermal nonequilibrium is present in the boundary layer even though the wall boundary conditions for the simulation puts the two temperatures into thermal equilibrium. The no-slip condition is present for the u velocity component and wall normal blowing is less than 1 m/s. The only significant carbon species in the boundary layer is CO which has a mass fraction of 0.123 at the wall and decreases quickly away from the wall. The temperatures are high enough for dissociation of oxygen to occur but not high enough for nitrogen to dissociate significantly.

Figures 3(a)–3(f) give a comparison of the perturbation amplitude for a second mode disturbance ($\beta = 0$) of translation-rotation temperature, vibration temperature, pressure and density of N_2, O_2 and CO respectively. For T and T_V it can be seen that at the wall the boundary conditions are different. For LST the

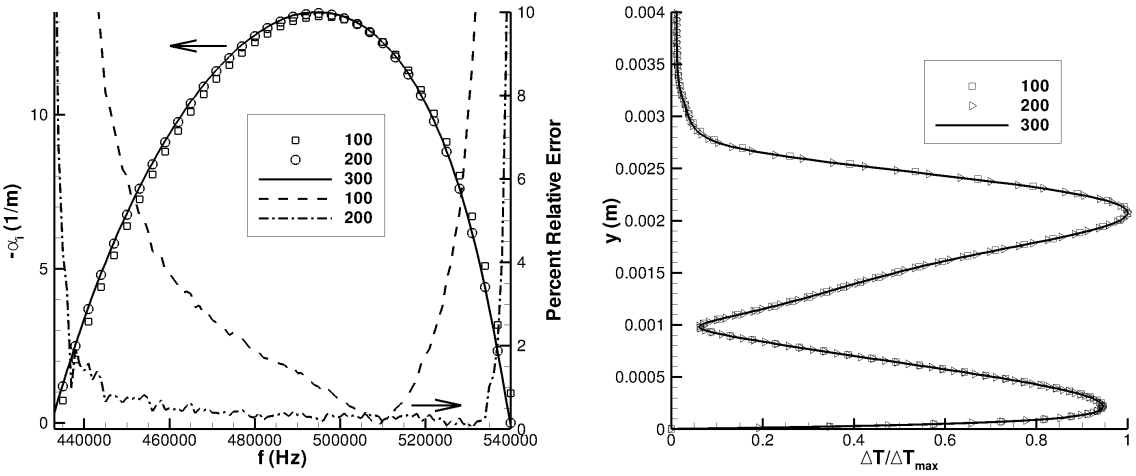

(a) (b)

Figure 1. Comparison of (a) amplification rate and (b) temperature perturbation amplitude for three different grid densities.

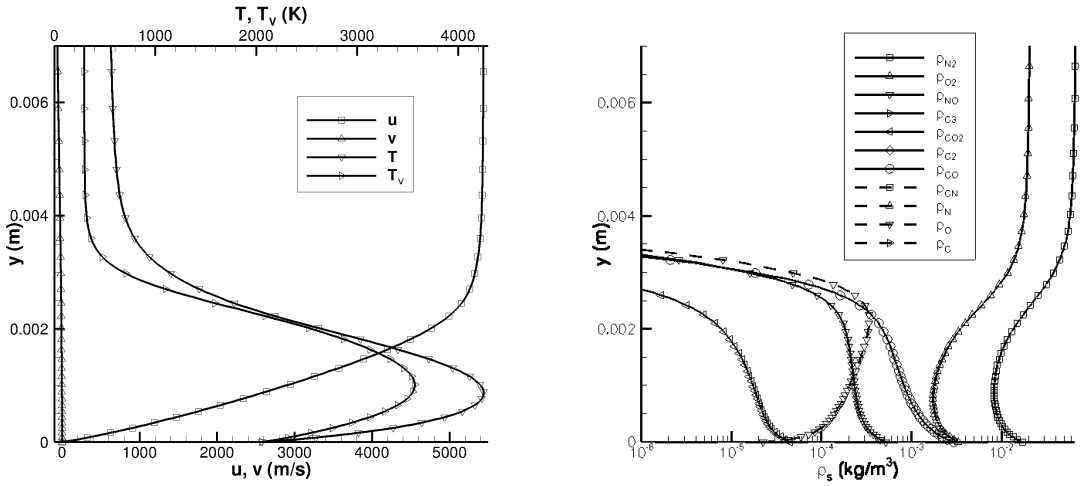

(a) (b)

Figure 2. Boundary layer profiles at s=0.564 m for (a) velocity and temperature, and (b) species density.

amplitudes are zero and for DNS the amplitudes are not zero. The comparison is good at the wall but near the edge of the boundary layer LST predicts a larger perturbation amplitude. This could be due to curvature effects as they are neglected in the LST code but are not neglected in the DNS results. The pressure perturbation amplitude has only a small difference away from the wall. For the density of N_2 and O_2 the slope at the wall is different which leads to a slight difference near the wall. The comparison for density of CO is nearly the same except for the slope at the wall. These differences are most likely due to the wall conditions since the slope at the wall for each species in the DNS simulation is determined by that specific species conservation equation.

The comparison of the disturbance phase is given in Figures 3(g)–3(l). Once again the difference due to the different boundary conditions can be seen for each eigenvector phase near the wall. For T and T_V the LST code accurately matches the 180° phase change near $y = 0.001$ m. This phase change occurs between the two amplitude peaks. For T_V there is an oscillation in the phase near $y = 0.003$ m. This oscillation did

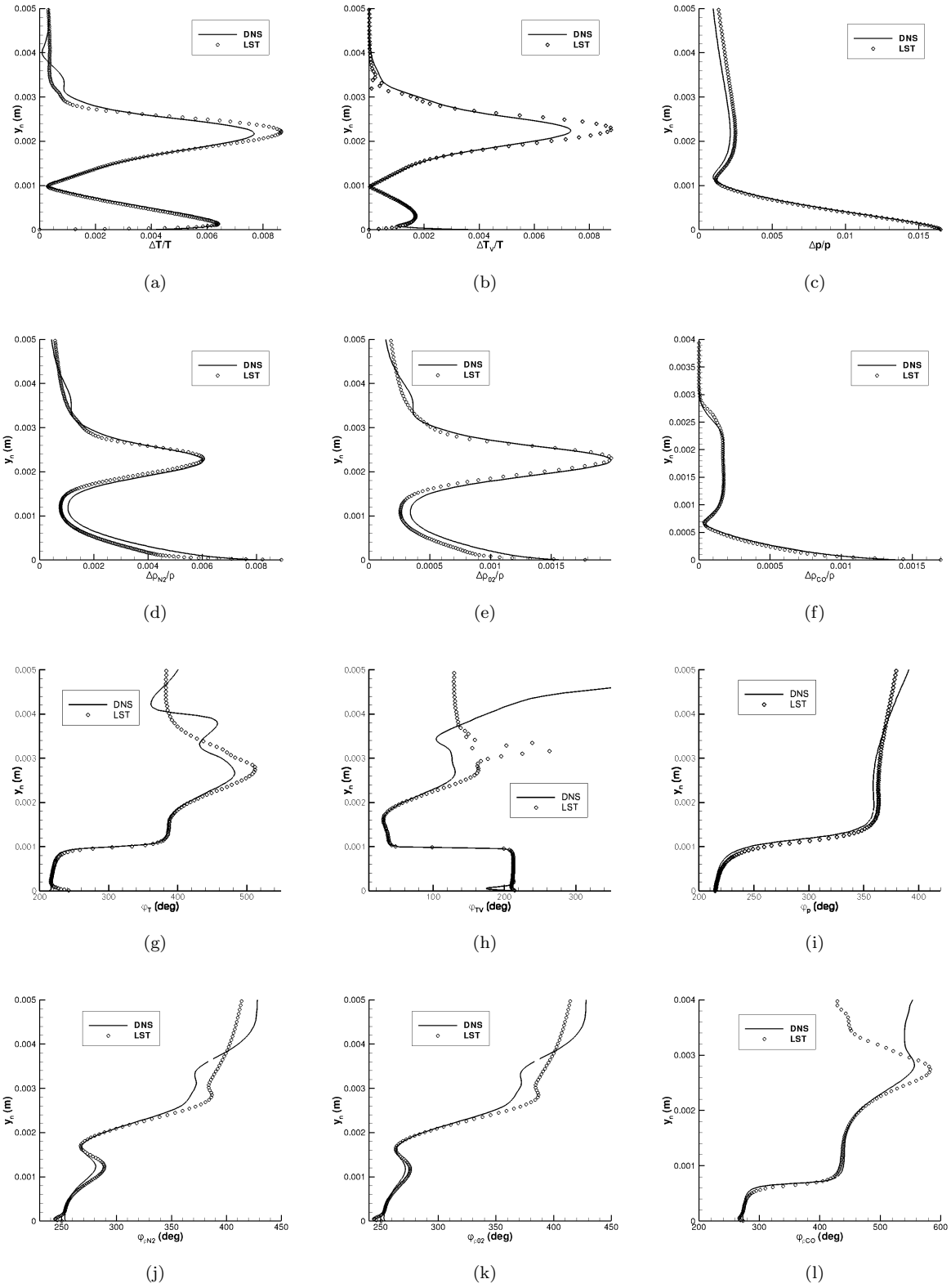

Figure 3. Eigenfunction comparison for a 525 kHz second mode disturbance between DNS and LST at s=0.564 m for (a)-(f) perturbation amplitude and (g)-(l) their corresponding phase.

not occur in the T_V eigenvector for other tested boundary layer profiles so it is thought to be from numerical error and is not physical. For each density the comparison of the phase is good near the wall but differs away from the wall. This is due to the waves outside the boundary layer in the DNS simulation which are not present in LST. Considering that the two stability methods compute the eigenvectors in a much different way and that the boundary conditions are different the overall comparison is quite good and gives confidence that both methods have been implemented correctly.

It is also possible to compare the growth rate and wavenumber i.e. the real and imaginary parts of alpha obtained from LST to a DNS simulation. It is difficult to make a comparison at a single location so multiple streamwise locations are used. Figure 4(a) shows the wavenumber comparison for a 525 kHz second mode disturbance where s is the streamwise distance measured from the stagnation point. The wavenumber computed from LST compares well with the DNS simulation. Upstream near $s = 0.2$ m the 525 kHz is just becoming unstable in the DNS simulation so the second mode is not dominant yet. Moving downstream the second mode starts to become dominant as witnessed by the lessening fluctuations and the comparison between the two is much better. A similar trend is seen in Figure 4(b) where a comparison of the growth rate is given. Upstream there are large fluctuations in growth rate that damp downstream. The growth rate of the LST code moves through the middle of the fluctuations as it should. Even though the wall boundary conditions are different for the two methods and the LST code does not contain the transverse curvature metrics the agreement is quite good.

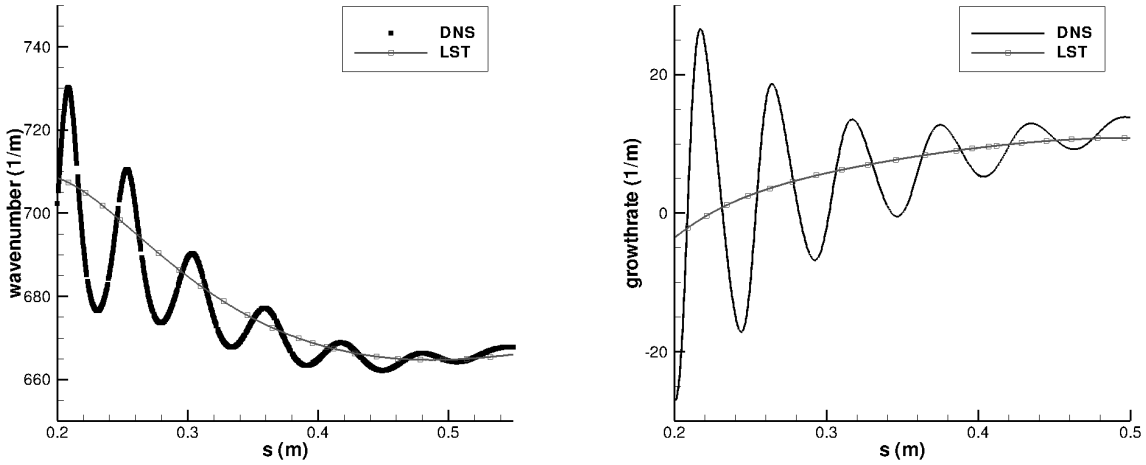

(a) (b)

Figure 4. LST comparison to DNS for the (a) wavenumber and (b) growth rate of a 525 kHz second mode disturbance.

VI. Direct Numerical Simulation of $M_\infty = 15.99$ Blunt Cone

A. Steady State Solution of $M_\infty = 15.99$ Blunt Cone

A direct numerical simulation was performed to study hypersonic boundary layer receptivity with graphite ablation induced outgassing effects over a cone frustum. The geometry is a sphere cone with a nose radius of 0.00635 m and a cone half angle of 7°. The freestream conditions are listed in Table 2. The cone axis is aligned with the freestream flow yielding an angle of attack equal to zero. The freestream unit Reynolds number and stagnation enthalpy are $Re_u = 7.3 \times 10^6$ $/m$ and $h_{o,\infty} = 15.3$ MJ/kg respectively. This is a high enthalpy case where thermochemical nonequilibrium effects are significant and still present well downstream of the nose. Figure 5 shows the computational domain where the shock is colored black and the wall and the outlet are gray. Since it was assumed *a priori* that the dominate instability mode for this configuration would be the second mode a two dimensional simulation was performed to minimize the required computing resources.

Table 2. Freestream conditions.

M_∞	15.99
ρ_∞	$2.4093 \times 10^{-2}\ kg/m^3$
P_∞	$2026.0\ N/m^2$
C_{N_2}	0.7635
C_{O_2}	0.2365

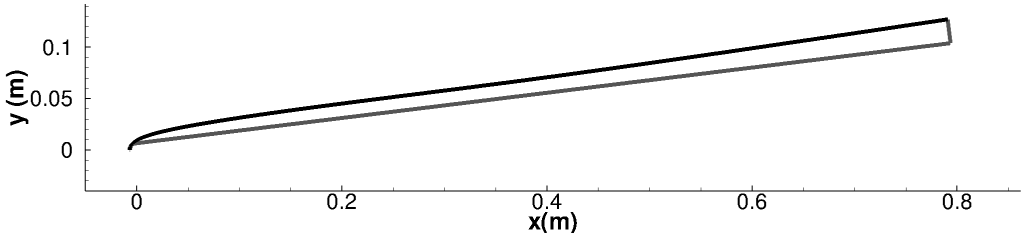

(a)

Figure 5. Simulation domain for 7° half angle blunt cone. The shock is black and the wall and outlet are gray.

A grid convergence study was performed to ensure that the computational grid was sufficient to capture the meanflow as well as the unsteady flow field characteristics. The grid density in the streamwise direction was chosen to adequately resolve the highest imposed perturbation frequency (525 kHz). There are 3155 grid points in the streamwise direction. The grid in the wall normal direction was tested with 240 points and 480 points. The meanflow solution was computed for both cases and then unsteady computations were performed for both cases. The relative error between the two grids for the highest imposed frequency surface pressure perturbation amplitude was around 5% for the length of the domain and the error decreased for the lower frequencies. Since the discretization scheme described in Section III has a global error of order four a 960 point grid will have a relative percent error around (5/16)% which would yield a grid converged solution for the 480 wall normal point grid. For the following simulations the 480 point wall normal grid is used.

Figure 14 and 15 show steady state contours of translation-rotation temperature, vibration temperature, oxygen and atomic oxygen for most of the cone frustum. For all these figures the top of the domain is the shock location which moves away from the wall as the flow moves downstream. Most of the shock layer is blue for both temperatures which represents the inviscid region between the boundary layer and the shock wave. Similarly this region can be seen in the plots of atomic oxygen mass fraction. As the flow moves downstream atomic oxygen is recombining to form oxygen. A more exhaustive visualization of the steady state is given in Mortensen and Zhong.[15]

To help visualize the blowing profile caused by chemical reactions at the surface, Figure 6(a) shows the wall mass flux per area nondimensionalized by the freestream mass flux per area. This nondimensionalization is chosen because it is common in stability literature with wall blowing. The largest mass flux is at the stagnation point (approximately 1% of the freestream mass flux) where the oxidation reactions as well as the sublimation reactions are all significant. The wiggle near the nose of the cone is located directly downstream of where the sphere and the cone join. This discontinuity in the surface curvature is likely the cause for the wiggle and the appearance of the wiggle is exaggerated by use of a logarithmic scale. The rapid drop of wall mass flux corresponds to the rapid decrease in sublimation which is shown in Figure 7. The fact that there is still wall blowing in the cone frustum is due to the oxidation reactions.

Unlike many simulations of hypersonic boundary layer stability the wall temperature is not constant nor is the adiabatic condition ($\frac{\partial T}{\partial n} = 0$) enforced. Rather a surface energy balance (Eq. (43)) is solved which yields a temperature profile shown in Figure 6(b). Recall that the surface is assumed to be in thermal equilibrium meaning $T_V = T$ at the surface. The temperature has a maximum at the stagnation point and then drops rapidly as the flow expands. It is important to solve for the surface temperature in hypersonic flows with ablation as the wall temperature directly determines the reaction rate and probability for oxidation. It also

plays a role in sublimation. In this case, as the wall temperature drops the wall mass flux drops as well. Note that the temperature of the wall is decreasing which corresponds to wall cooling which is destabilizing to second mode disturbances.

To help understand the chemical processes at the surface Figure 7 shows the mass fraction for each species at the surface. The species with the largest mass fraction at the surface is N_2 but it does not react with the surface. The next largest mass fraction is CO. Recall from Eqs. (31) and (32) that the carbon surface can react with O and O_2 to form CO. These two reactions are the dominate reactions for the entire length of the surface i.e. they are responsible for the most mass loss due to ablation at the surface. Sublimation of C_3 (Eq. (38)) is an order of magnitude less than CO at the stagnation point. In the sphere region it is the dominate sublimation product. There is a significant mass fraction of CN at the surface even though a nitridation reaction is not taken into account in the surface chemistry model. CN at the surface is due to reactions of ablation products with N_2 and NO. For the entire length of the cone frustrum CO is the most numerous species containing carbon. This shows that CO is the species most likely to have the largest effect on boundary layer receptivity and stability over the cone frustum.

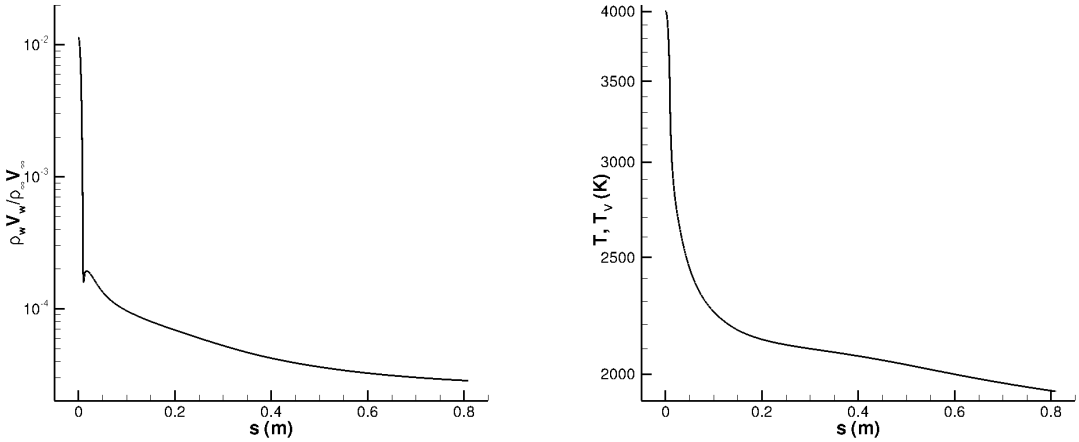

(a) (b)

Figure 6. Surface (a) nondimensional mass flux and (b) temperature. The surface is in thermal equilibrium.

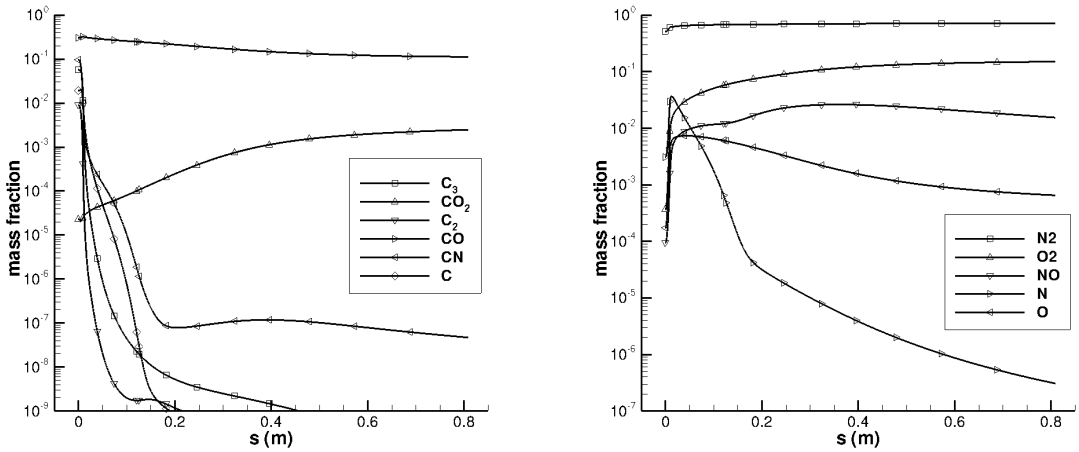

(a) (b)

Figure 7. Surface mass fraction for (a) carbon containing species and (b) air species.

1. *Ideal Gas Steady Solutions*

Three separate steady solutions were computed for receptivity simulations. The first is the full thermochemical nonequilibrium shock-fitting method with graphite ablation. The other two cases are ideal gas cases which use the same nonequilibrium code with the source terms turned off, the vibration energy held constant, and the mass fractions held to their freestream value. This is done so the viscosity, thermal conductivity, &c. are calculated the exact same way for the nonequilibrium and ideal gas cases. The first ideal gas case uses the temperature at the wall boundary from the thermochemical nonequilibrium graphite ablation case with the no slip boundary condition. The second ideal gas case matches the wall temperature as well as the wall mass flux of the thermochemical nonequilibrium graphite ablation case. This is done to test the effects of thermochemical nonequilibrium and wall mass flux on boundary layer stability. For ease of discussion the two ideal gas cases will be called 'ideal gas' and 'ideal gas blowing' while the full thermochemical nonequilibrium ablation case will be called 'real gas'.

Figure 8 compares the shock layer profiles for each of the three cases at three separate streamwise locations. u_t represents the velocity tangent to the surface and y_n is the wall normal coordinate. These three profiles are all located on the cone frustum. The location of the shock height is at the top of each profile. Both ideal gas cases have a larger shock height than the real gas case and the difference becomes less moving downstream as expected. The two ideal gas cases have similar boundary layer profiles and the real gas profile looks like it is approaching the ideal gas profile downstream as real gas effects become less acute. Similarly for temperature, the ideal gas cases are similar and the translation-rotation temperature is getting close to the ideal gas solution downstream.

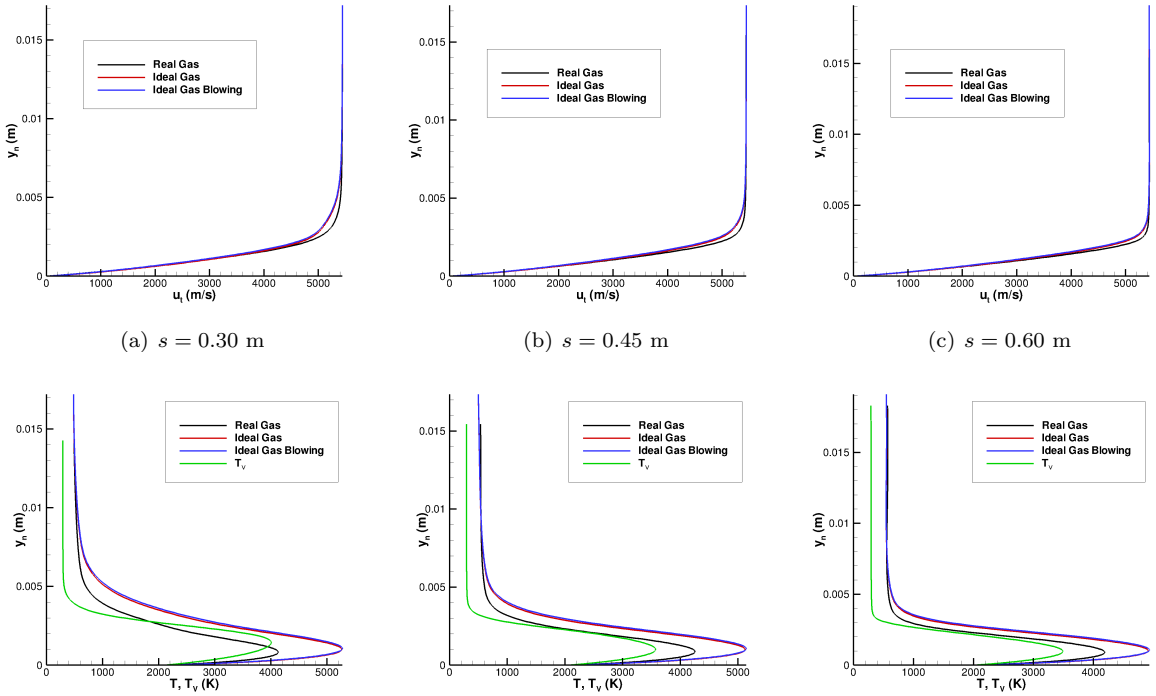

(a) $s = 0.30$ m (b) $s = 0.45$ m (c) $s = 0.60$ m

(d) $s = 0.30$ m (e) $s = 0.45$ m (f) $s = 0.60$ m

Figure 8. Steady state profile comparison between the three simulation cases for select streamwise locations. Velocity is tangent to the surface.

B. Hypersonic Boundary Layer Receptivity Results

After computing the steady solutions, freestream disturbances were imposed in the freestream to find how the boundary layer behaved in the presence of graphite ablation and thermochemical nonequilibrium. The freestream disturbances imposed are weak planar fast acoustic waves in the freestream before reaching the

shock at a zero incidence angle. The freestream variables can be written as the summation of the mean flow value and an oscillating component as

$$V_\infty = \begin{bmatrix} \rho_{1,\infty} \\ \vdots \\ \rho_{ns,\infty} \\ u_{1,\infty} \\ u_{2,\infty} \\ u_{3,\infty} \end{bmatrix} = \begin{bmatrix} \bar{\rho}_{1,\infty} \\ \vdots \\ \bar{\rho}_{ns,\infty} \\ \bar{u}_{1,\infty} \\ \bar{u}_{2,\infty} \\ \bar{u}_{3,\infty} \end{bmatrix} + \begin{bmatrix} \Delta\rho_{1,\infty} \\ \vdots \\ \Delta\rho_{ns,\infty} \\ \Delta u_{1,\infty} \\ \Delta u_{2,\infty} \\ \Delta u_{3,\infty} \end{bmatrix} \exp\left(i\left(k_x\left(x - \left(u_{1,\infty} + c_\infty\right)\right)t\right)\right) \tag{48}$$

where the disturbance amplitudes are defined by

$$\epsilon = \frac{\Delta P_\infty}{\gamma_\infty p_\infty} = \frac{\Delta\rho_\infty}{\rho_\infty} = \frac{\Delta u_{1,\infty}}{\gamma_\infty c_\infty}. \tag{49}$$

Here γ_∞ is the ratio of specific heats in the freestream and c_∞ is the speed of sound in the freestream. $\epsilon = 5 \times 10^{-4}$ and seven frequencies are imposed starting with a base frequency of 75 kHz. Each frequency is a multiple of this base and the last frequency is 525 kHz. All frequencies are imposed simultaneously and their phases are set randomly.

For each of the three cases different unsteady wall boundary conditions were imposed. Each case uses pressure extrapolation to set the disturbance wall pressure. For the real gas case the surface mass balance as well as the surface energy balance are used as boundary conditions. This means that the wall normal velocity will fluctuate as well as the wall temperature. For the ideal gas case the no slip condition is enforced on the disturbances and $\Delta T_w = 0$. For the ideal gas blowing case the mass flux is forced to remain constant and $\Delta T_w = 0$. When enforcing the mass flux to remain constant the wall normal velocity must fluctuate because density will fluctuate at the surface (recall Eq. (46)).

Figures 16–20 show an instantaneous snapshot of the real gas perturbed flow field for the 525 kHz frequency disturbance of pressure, translation-rotation temperature, vibration temperature, oxygen and atomic oxygen respectively. The 525 kHz frequency is shown because it is the most unstable frequency. Note that the scales for the different figures are not the same so colors cannot be compared between figures. Figure 3 which was used to validate the LST code came from the unsteady data set displayed here so it represents the mode shapes seen in the instantaneous flow.

For second mode disturbances the pressure perturbation is a maximum at the surface which can be seen in Figs. 16(a)–16(h). For both temperatures there is a high perturbation outside of the boundary layer that moves closer to the boundary layer edge and decreases in magnitude as the flow moves downstream. Eventually this peak disappears. For both temperatures the maximum perturbation amplitude is the same order of magnitude. The translation-rotation temperature has two peaks inside the boundary layer: one near the wall and one near the boundary layer edge. Like the translation rotation temperature the vibration temperature has two peaks inside the boundary layer but the peak near the boundary layer edge is much larger. The contours of oxygen and atomic oxygen also show second mode disturbances near the surface that increase in strength as the flow moves downstream.

An unstable frequency range and the corresponding phase velocity computed using LST for three streamwise locations along the cone frustum is given in Figure 9. For $s = 0.30$ m and $s = 0.45$ m the most unstable frequency is near 510 kHz but for $s = 0.45$ m it is near 490 kHz. The maximum amplification factor increases in the downstream direction. The unstable frequency range also increases while moving downstream. For all three cases the phase velocity for the unstable frequency range decreases as the frequency increases. The 525 kHz frequency used to perturb the meanflow in the DNS simulation falls inside the unstable frequency range for each of these streamwise locations indicating that it should grow exponentially. The 450 kHz disturbance is in the unstable range for $s = 0.60$ m so it should become unstable in the DNS simulation but not until the end of the domain.

Figure 10 gives a comparison of the wall pressure perturbation amplitude for each of the three cases. It should be noted that the end of the domain (approximately x=0.6m to x=0.8 m) for the real gas simulation has perturbation amplitudes near 10% of the freestream values. This means that the flow is no longer linear and the two dimensional assumption for the flow field disturbances is no longer valid. For all three cases there is some transient growth for the higher imposed frequencies near the beginning of the cone. Also, for all three cases frequencies below 450 kHz are stable. For the real gas case the most unstable frequency is

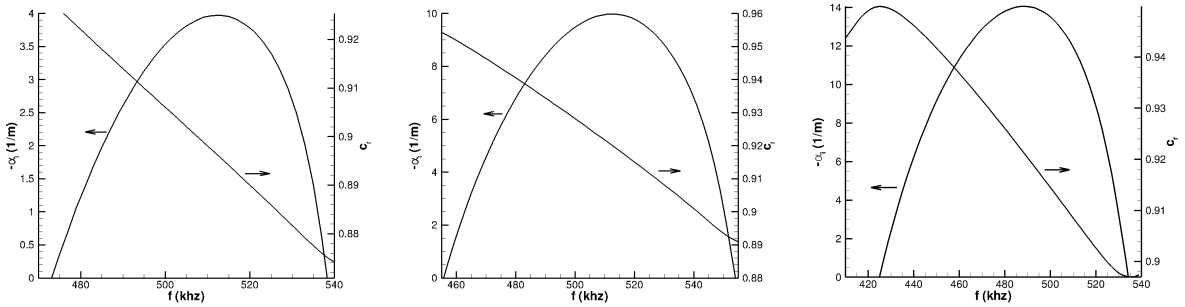

(a) $s = 0.30$ m (b) $s = 0.45$ m (c) $s = 0.60$ m

Figure 9. Unstable frequency range and corresponding phase velocity nondimensionalized by the boundary layer edge velocity. Obtained from LST.

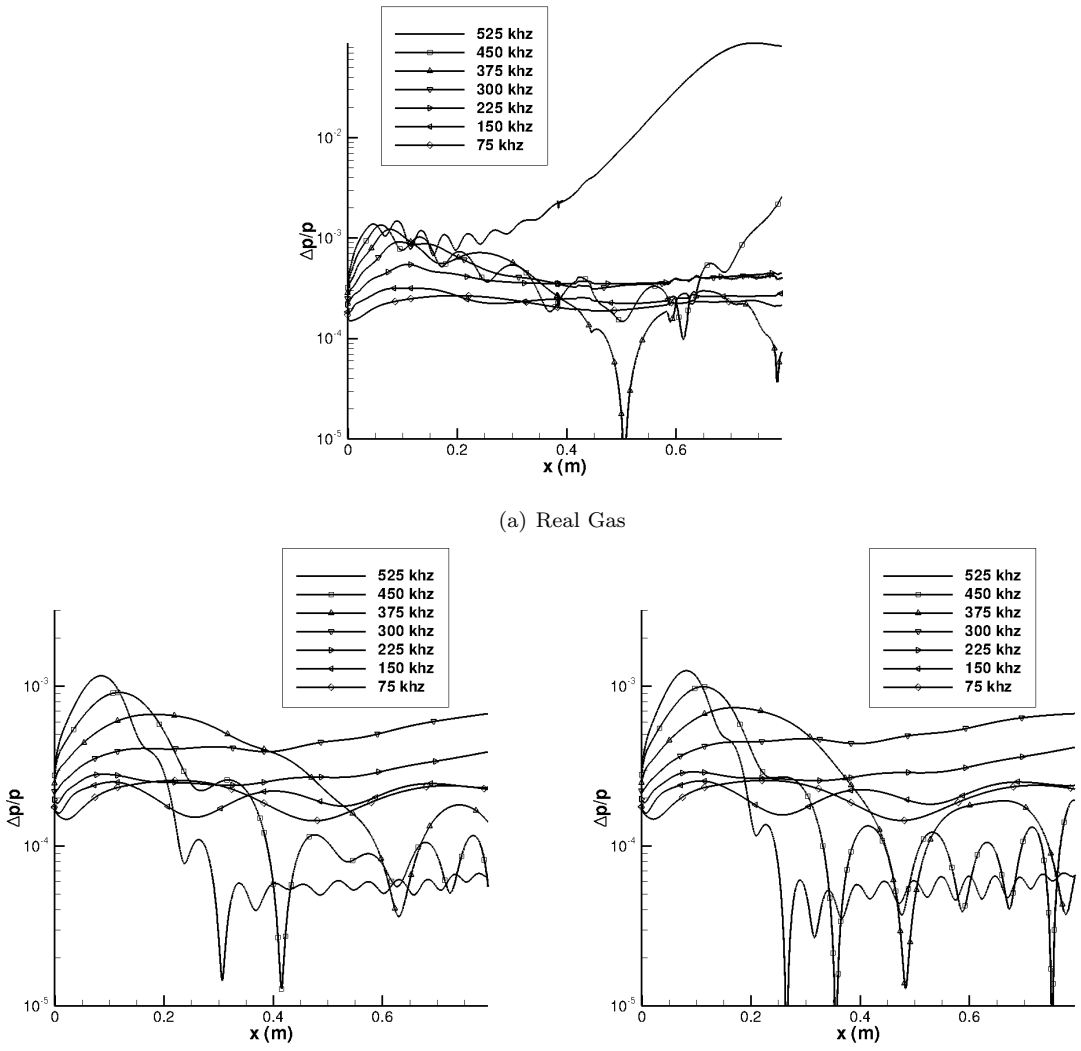

(a) Real Gas

(b) Ideal Gas (c) Ideal Gas with Blowing

Figure 10. Pressure perturbation amplitude at the wall computed by DNS.

525 kHz and its exponential growth starts around x=0.2 m and is unstable almost to the end of the domain. This is a large unstable region of approximately 0.6 m. The 450 kHz disturbance becomes unstable near the end of the domain but by this time the disturbance flow field has become nonlinear. For the ideal gas cases the 525 kHz frequency and the 450 kHz frequency become slightly unstable downstream of x=0.4 m but the growth is much smaller than for the real gas case. This shows that the unstable frequency range starts further upstream for the real gas case than for either ideal gas case and also the real gas frequencies have a larger growth rate. Since blowing rates are low (Figure 6(a)) on the cone frustum and blowing is imposed for one of the ideal gas cases it is possible that the differences between the cases are more dependent on real gas effects i.e. gas phase reactions and thermal nonequilibrium than on wall blowing due to surface chemistry.

The perturbation amplitudes for each carbon species at the wall is shown in Figure 11. As none of the carbon species diffuse very far from the wall it is difficult to visualize their perturbations except to plot them along the surface. The two most significant species amplitudes are CO and CO_2. This follows the fact that CO and CO_2 are the two carbon species that have the most mass at the wall in the steady solution as seen in Figure 7. The maximum amplitudes for these two species occur at the wall where only a slight peak is seen away from the wall. This is unlike N_2 and O_2 where there is a high amplitude near the wall and a high amplitude near the boundary layer edge as well (see Figure 3). It is interesting to note that the initial transient growth seen for Δp at 525 kHz is only seen slightly in the species densities of CO and CO2 and is not seen in the other species. This could simply be due to the fact that the mass fraction is already decreasing so quickly at the wall (Figure 7) for all carbon species except CO and CO_2 that transient growth has little effect for these species.

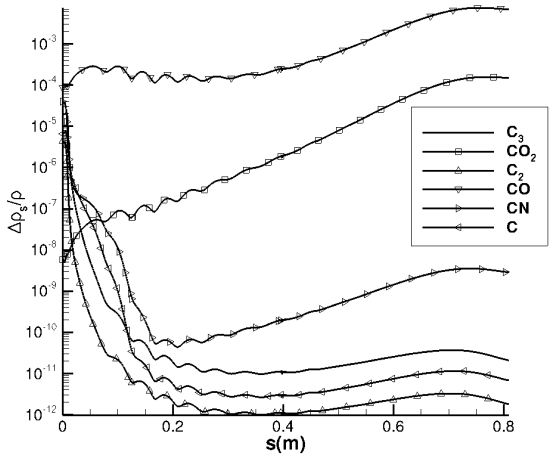

Figure 11. Perturbation of species density for each carbon species at 525 kHz. Perturbed quantities taken at the wall and obtained from DNS.

It is possible to compute the growth rate, wavenumber and phase speed of each disturbance frequency containing multiple boundary layer modes and compare them to the real gas LST predictions for a single boundary layer mode. In the DNS the growth rate, wavenumber and phase speed are computed from

$$-\alpha_i = \frac{1}{\Delta H(f_n)} \frac{d\Delta H(f_n)}{ds} \tag{50}$$

$$\alpha_r = -\frac{d\phi(f_n)}{ds} \tag{51}$$

$$c_r = \frac{2\pi f_n}{\alpha_r} \tag{52}$$

where f_n represents a single dimensional frequency, s is the streamwise coordinate, ΔH is the amplitude of a perturbed variable, and ϕ is the phase of the specified perturbed variable. Here pressure at the wall is used as the perturbed value. As the 525 kHz disturbance shows predominantly second mode behavior it is of the most interest and best compares to LST predictions. For LST predictions α was traced downstream starting with a known second mode value for α.

A comparison of the growth rate for the 525 kHz disturbance is given in Figure 12. The oscillations in the DNS growth rates comes from multiple competing modes that are all present simultaneously during the simulation where the LST growth rate is smooth because it is computing one single mode. For all three cases growth can be seen near $s = 0$ which represents the stagnation location. This growth is most likely transient growth and not modal growth as the LST calculations do not predict this growth. The real gas DNS simulation shows modal growth starting near $s = 0.2$ m that compares well with LST predictions. The two methods begin to diverge downstream where the DNS disturbance amplitudes are large enough where nonlinear behavior cannot be neglected. Downstream the oscillations in the DNS growth rate die out showing that the second mode is becoming the dominant boundary layer mode. This behavior is not seen in the ideal gas cases because there is no dominant mode so the oscillations do not decrease. For both ideal gas cases it is difficult to say if there is any growth because the growth rate is oscillating close to zero.

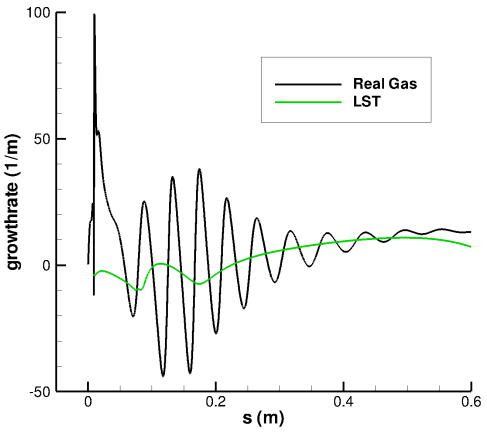

(a) Real Gas DNS and LST

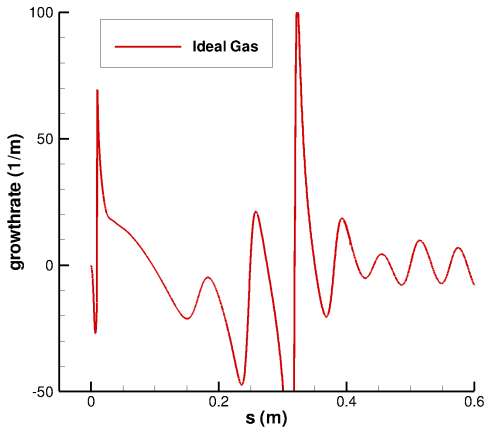

(b) Ideal Gas DNS

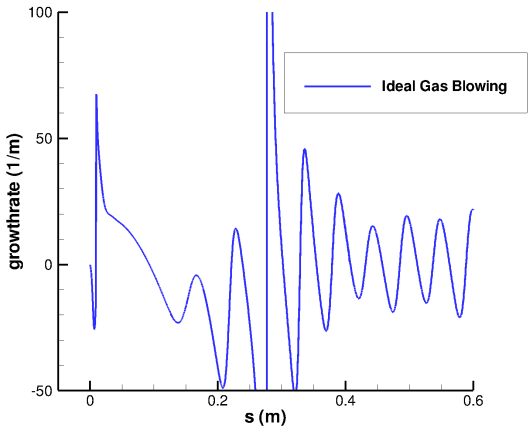

(c) Ideal Gas Blowing DNS

Figure 12. Growth rate comparison for the 525 kHz disturbance.

The wavenumber and phase speed for the 525 kHz disturbance is shown for all three cases in Figure 13. An LST comparison is given for the real gas case and the phase speed is nondimensionalized by the freestream velocity. Once again oscillations are seen in the DNS simulation that die out for the real gas case downstream indicating a dominating boundary layer mode. For both the wavenumber and the phase speed the LST and DNS results compare well which helps to give confidence in the results for both methods. It is interesting to note that the boundary layer wave for the real gas case has a nondimensional phase speed near unity at the domain entrance which is indicative of an entropy/vorticity wave where for the ideal gas cases the

phase speed is around 1.1 indicating a fast acoustic wave. Recall that freestream fast acoustic waves were used in the freestream to perturb the steady flow. Logically it would seem that with fast acoustic freestream forcing the incoming wave would be predominantly fast acoustic as well but it is possible that real gas effects or surface chemistry effects are exciting the entropy/vorticity wave more strongly than the ideal gas cases. Following the phase velocity downstream for the two ideal gas cases shows the phase velocity drop as it likely approaches a synchronization point with the slow acoustic mode and then increases back to the fast acoustic phase velocity. For the real gas simulation the phase velocity drops slightly below 0.9 and remains there for the length of the domain. Further analytical inspection needs to be done to find out precisely what physical mechanisms are at play here.

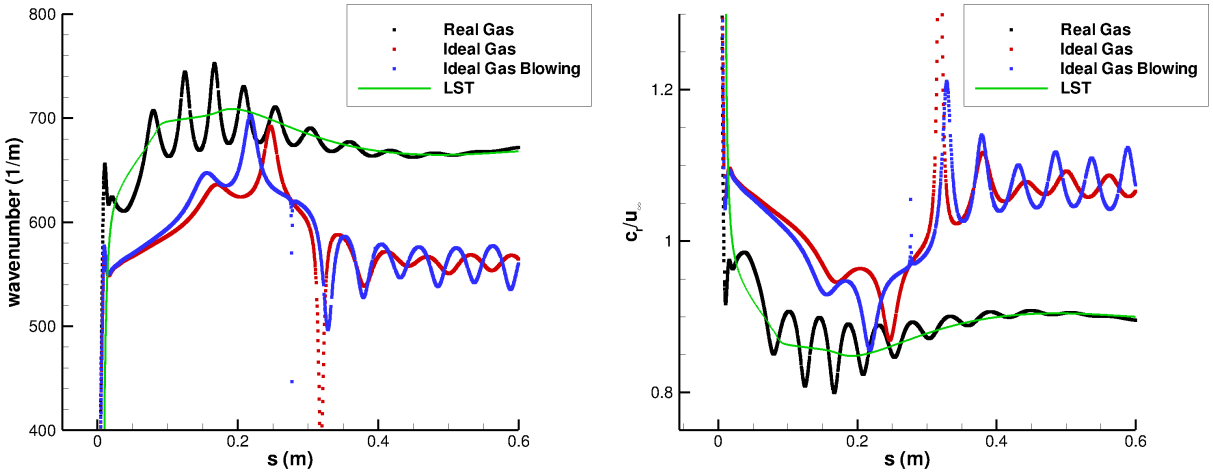

(a) (b)

Figure 13. Comparison of (a) wavenumber and (b) phase velocity nondimensionalized by the freestream velocity for the 525 kHz disturbance.

VII. Conclusion

A new thermochemical nonequilibrium linear stability theory code has been developed and validated. The linear stability theory code follows the work of Hudson. An eleven species gas model is used where five species model air and six more species are used to model graphite ablation effects. The code was validated with results from a direct numerical simulation of flow field disturbances over a blunt cone. The boundary conditions were different for the two methods but the comparison of the eigenfunctions as well as the wavenumber and growth rate are good.

A direct numerical simulation was run for a 7° half angle blunt cone at Mach 15.99 to find how graphite ablation induced outgassing affects boundary layer stability over a cone frustum. Three cases were run: real gas, ideal gas, and ideal gas with blowing. The real gas simulation showed second mode disturbances for the 525 kHz fast acoustic wave imposed in the freestream. Neither ideal gas simulation showed significant second mode growth for any of the frequencies simulated. Real gas effects moved the instability region upstream when compared to ideal gas computations. The results show that real gas and ablation induced outgassing effects for this case significantly alter boundary layer receptivity and stability.

VIII. Future Work

Future work for the LST code includes linearizing the surface chemistry boundary conditions and adding them to the code. Also, the current LST code is formulated for a flat plate so the transverse curvature metrics need to be added to accurately account for axisymmetric geometries. For both codes future work includes updating the gas phase chemistry models with up to date forward reaction rates and equilibrium constants.

The finite rate surface chemistry model from Zhluktov and Abe[36] will be added to test how different surface chemistry models affect boundary layer receptivity and stability. The current direct numerical simulation results for a cone frustum will be further analyzed using linear stability theory. A good representative geometry for re-entry vehicles with ablative heat shields is a sphere. In the future we would like to study how ablation affects boundary layer transition on a sphere and specifically the effects on three dimensional boundary layer instabilities.

Acknowledgements

The research was supported in part by the AFOSR/NASA National Center for Hypersonic Research in Laminar-Turbulent Transition and also the Department of Defense (DoD) through the National Defense Science & Engineering Graduate Fellowship (NDSEG) Program. The computations are mainly run on XSEDE resources provided by TACC under grant number TG-ASC100002 supported in part by the National Science Foundation. The views and conclusions contained herein are those of the authors and should not be interpreted as necessarily representing the official policies or endorsements either expressed or implied, of the Air Force Office of Scientific Research or the U.S. Government.

References

[1]Ungar, E., "Ablation Thermal Protection Systems," *Science*, Vol. 158, No. 3802, 1967, pp. 740–744.

[2]Mack, L., "Boundary Layer Linear Stability Theory," AGARD report No. 709, 1984.

[3]Malik, M., "Numerical Methods for Hypersonic Boundary Layer Stability," *Journal of Computational Physics*, Vol. 86, No. 2, 1990, pp. 376–413.

[4]Chang, C., Vinh, H., and Malik, M., "Hypersonic Boundary-Layer Stability with Chemical Reactions," *AIAA 1997-2012*, 1997.

[5]Stuckert, G. and Reed, H., "Linear Disturbances in Hypersonic, Chemically Reacting Shock Layers," *AIAA Journal*, Vol. 32, No. 7, 1994, pp. 1384–1393.

[6]Hudson, M., Chokani, N., and Candler, G., "Linear Stability of Hypersonic Flow in Thermochemical Nonequilibrium," *AIAA Journal*, Vol. 35, No. 6, 1997, pp. 958–964.

[7]Hudson, M., *Linear Stability Theory of Hypersonic, Chemically Reacting Viscous Flow*, Ph.D. thesis, North Caroline State University, 1996.

[8]Johnson, H., Seipp, T., and Candler, G., "Numerical Study of Hypersonic Reacting Boundary Layer Transition on Cones," *Physics of Fluids*, Vol. 10, No. 10, 1998, pp. 2676–2685.

[9]Ma, Y. and Zhong, X., "Receptivity to Freestream Disturbances of a Mach 10 Nonequilibrium Reacting Oxygen Flow over a Flat Plate," *AIAA 2004-0256*, 2004.

[10]Prakash, A., Parsons, N., Wang, X., and Zhong, X., "High-order Shock-fitting Methods for Direct Numerical Simulation of Hypersonic Flow with Chemical and Thermal Nonequilibrium," *Journal of Computational Physics*, Vol. 230, No. 23, 2011, pp. 8474–8507.

[11]Parsons, N., Zhong, X., Kim, J., and Eldredge, J., "High-order Shock-fitting Methods for Hypersonic Flow with Chemical and Thermal Nonequilibrium," *AIAA 2010-4997*, 2010.

[12]Johnson, H., Gronvall, J., and Candler, G., "Reacting Hypersonic Boundary Layer Stability with Blowing and Suction," *AIAA 2009-938*, 2009.

[13]Ghaffari, S., Marxen, O., Iaccarino, G., and Shaqfeh, E., "Numerical Simulations of Hypersonic Boundary-layer Instability with Wall Blowing," *AIAA 2010-706*, 2010.

[14]Li, F., Choudhari, M., Chang, C., and White, J., "Boundary Layer Transition over Blunt Hypersonic Vehicles Including Effects of Ablation-Induced Out-Gassing," *AIAA 2011-3303*, 2011.

[15]Mortensen, C. and Zhong, X., "Numerical Simulation of the Effects of Graphite Ablation on Hypersonic Boundary Layer Stability," *AIAA paper 2012-3150*, 2012.

[16]Wang, X. and Zhong, X., "A High-Order Shock-Fitting Non-Equilibrium Flow Solver for DNS of Srong Shock and Turbulence Interactions," *Seventh International Conference on Computational Fluid Dynamics*, ICCFD7-2307, 2012.

[17]Prakash, A., Parsons, N., Wang, X., and Zhong, X., "High-order Shock-fitting Methods for Hypersonic Flow with Chemical and Thermal Nonequilibrium," *AIAA 2010-4997*, 2010.

[18]Park, C., *Nonequilibrium Hypersonic Aerothermodynamics*, John Wiley & Sons Inc., New York, 1990.

[19]Dolton, T., Maurer, R., and Goldstein, H., "Thermodynamic Performance of Carbon in Hyperthermal Environments," *AIAA 68-754*, 1968.

[20]McBride, B., Heimel, S., Ehlers, J., and Gordon, S., "Thermodynamic Properties to 6000° for 210 Substances Involving the First 18 Elements," NASA SP-3001, NASA, 1963.

[21]Park, C., "On Convergence of Computation of Chemically Reacting Flows," *AIAA 85-0247*, 1985.

[22]Bhutta, B. and Lewis, C., "Low-to-High Altitude Predictions of Three-Dimensional Ablative Reentry Flowfields," *AIAA 92-0366*, 1992.

[23]Park, C., Howe, J., Jaffe, R., and Candler, G., "Chemical-Kinetic Problems of Future NASA Missions," *AIAA 91-0464*, 1991.

[24]Lee, J., "Basic Governing Equations for the Flight Regimes of Aeroassisted Orbital Transfer Vehicles," *Thermal Design of Aeroassisted Orbital Transfer Vehicles*, edited by H. F. Nelson, Vol. 96, AIAA, New York, 1985, pp. 3–53.

[25]Blottner, F., Johnson, M., and Ellis, M., "Chemically Reacting Gas Viscous Flow Program for Multi-Component Gas Mixtures," SC-RR-70-754, Sandia National Laboratories, 1971.

[26]Gupta, R., Lee, K., and Sutton, K., "Viscous-Shock-Layer Solutions with Coupled Radiation and Ablation Injection for Earth Entry," *AIAA 90-1697*, 1990.

[27]Candler, G., "Computation of Thermo-Chemical Nonequilibrium Martian Atmospheric Entry Flow," *AIAA 90-1695*, 1990.

[28]Wilke, C., "A Viscosity Equation for Gas Mixtures," *The Journal of Chemical Physics*, Vol. 18, No. 4, 1950, pp. 517–519.

[29]Zhong, X., "High-Order Finite-Difference Schemes for Numerical Simulation of Hypersonic Boundary-Layer Transition," *Journal of Computational Physics*, Vol. 144, No. 2, 1998, pp. 662–709.

[30]Klentzman, J., Ulker, E., and Tumin, A., "Projection of the Solution of the Linearized Navier-Stokes Equations in Reacting High Speed Boundary Layers onto Discrete Modes," *AIAA 2012-3149*, 2012.

[31]Chang, C.-L., "Langley Stability and Transition Analysis Code (LASTRAC) Version 1.2 User Manual," NASA TM-2004-213233, NASA, 2004.

[32]Anderson, E., Bai, Z., Bischof, C., Blackford, S., Demmel, J., Dongarra, J., Du Croz, J., Greenbaum, A., Hammarling, S., McKenney, A., and Sorensen, D., *LAPACK Users' Guide*, Society for Industrial and Applied Mathematics, Philadelphia, PA, 3rd ed., 1999.

[33]Park, C., "Effects of Atomic Oxygen on Graphite Ablation," *AIAA Journal*, Vol. 14, No. 11, 1976, pp. 1640–1642.

[34]Palmer, H. and Mordecai, S., *Chemistry and Physics of Carbon*, Marcel Dekker, Inc., NY, 1968.

[35]Baker, R., "Graphite Sublimation Chemistry Nonequilibrium Effects," *AIAA Journal*, Vol. 15, No. 10, 1977, pp. 1391–1397.

[36]Zhluktov, S. and Abe, T., "Viscous Shock-Layer Simulation of Airflow past Ablating Blunt Body with Carbon Surface," *Journal of Thermophysics and Heat Transfer*, Vol. 13, No. 1, 1999, pp. 50–59.

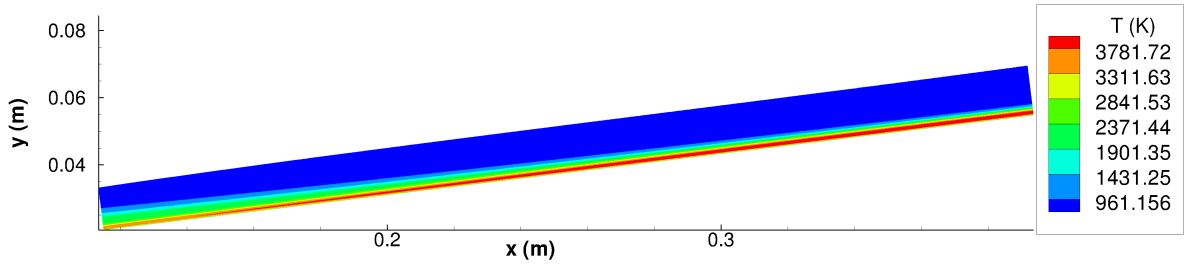

(a) Translation-rotation temperature

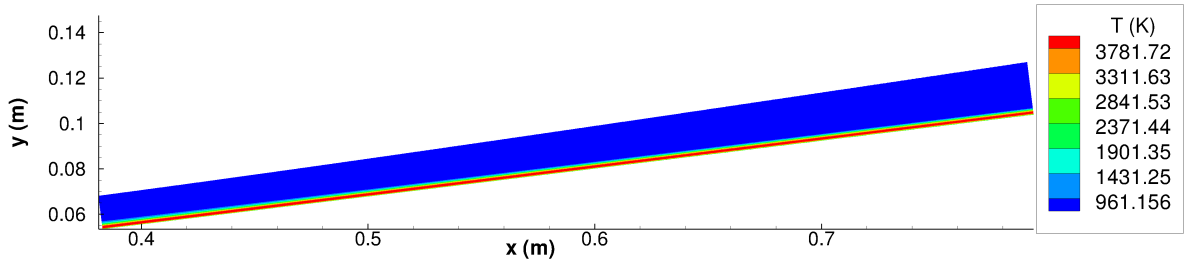

(b) Translation-rotation temperature

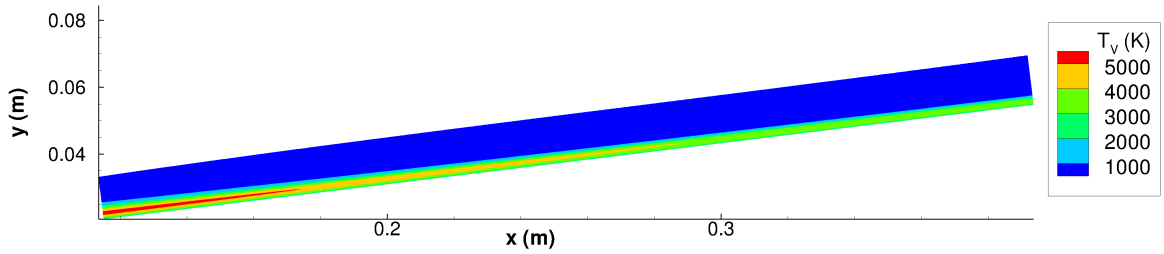

(c) Vibration temperature

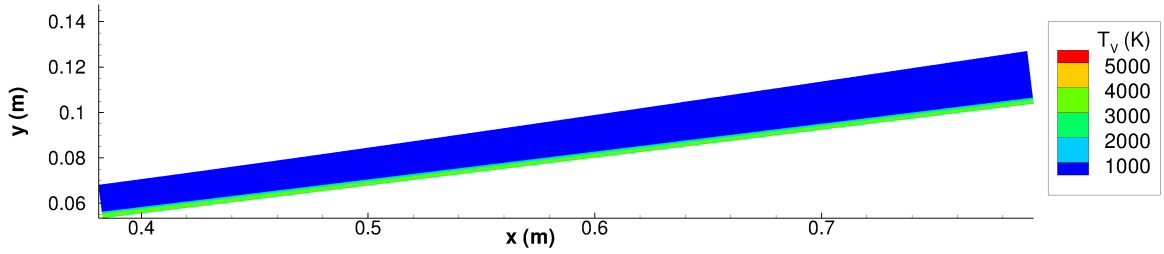

(d) Vibration temperature

Figure 14. Contour plots of T and T_V. Thermal nonequilibrium is present throughout the length of the domain.

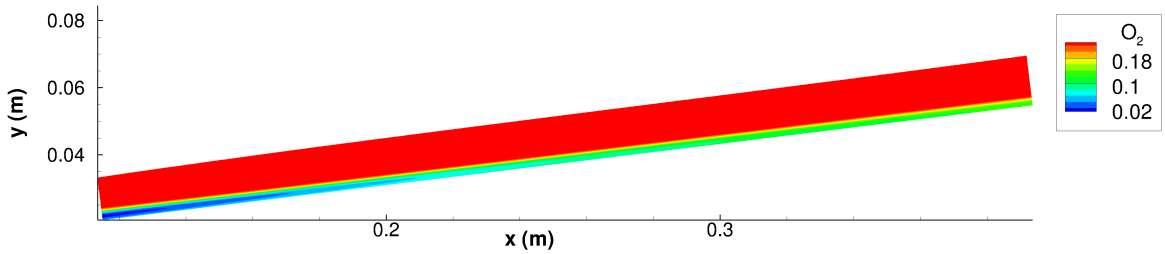

(a) O2 Mass Fraction

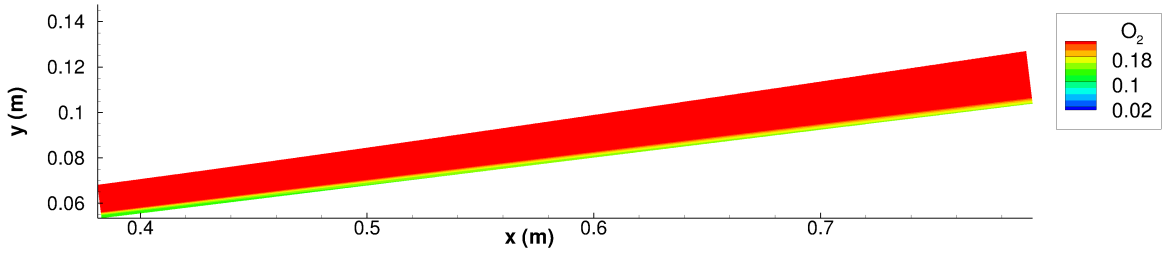

(b) O2 Mass Fraction

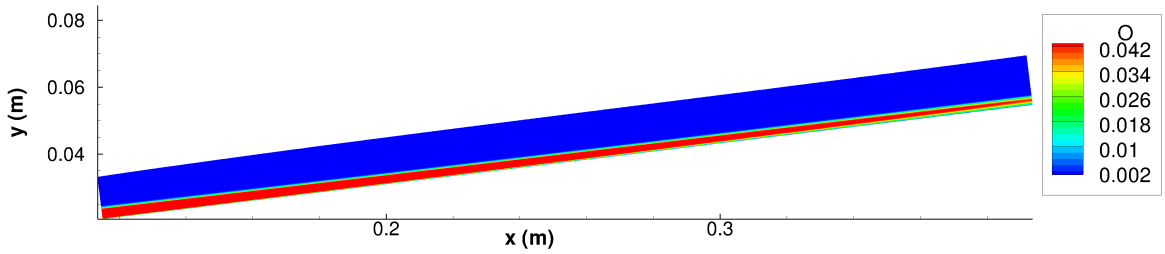

(c) O Mass Fraction

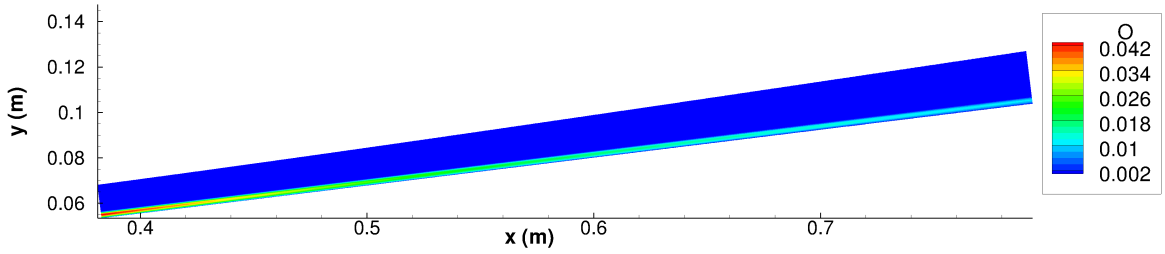

(d) O Mass Fraction

Figure 15. Contour plots of T and T_V. Thermal nonequilibrium is present throughout the length of the domain.

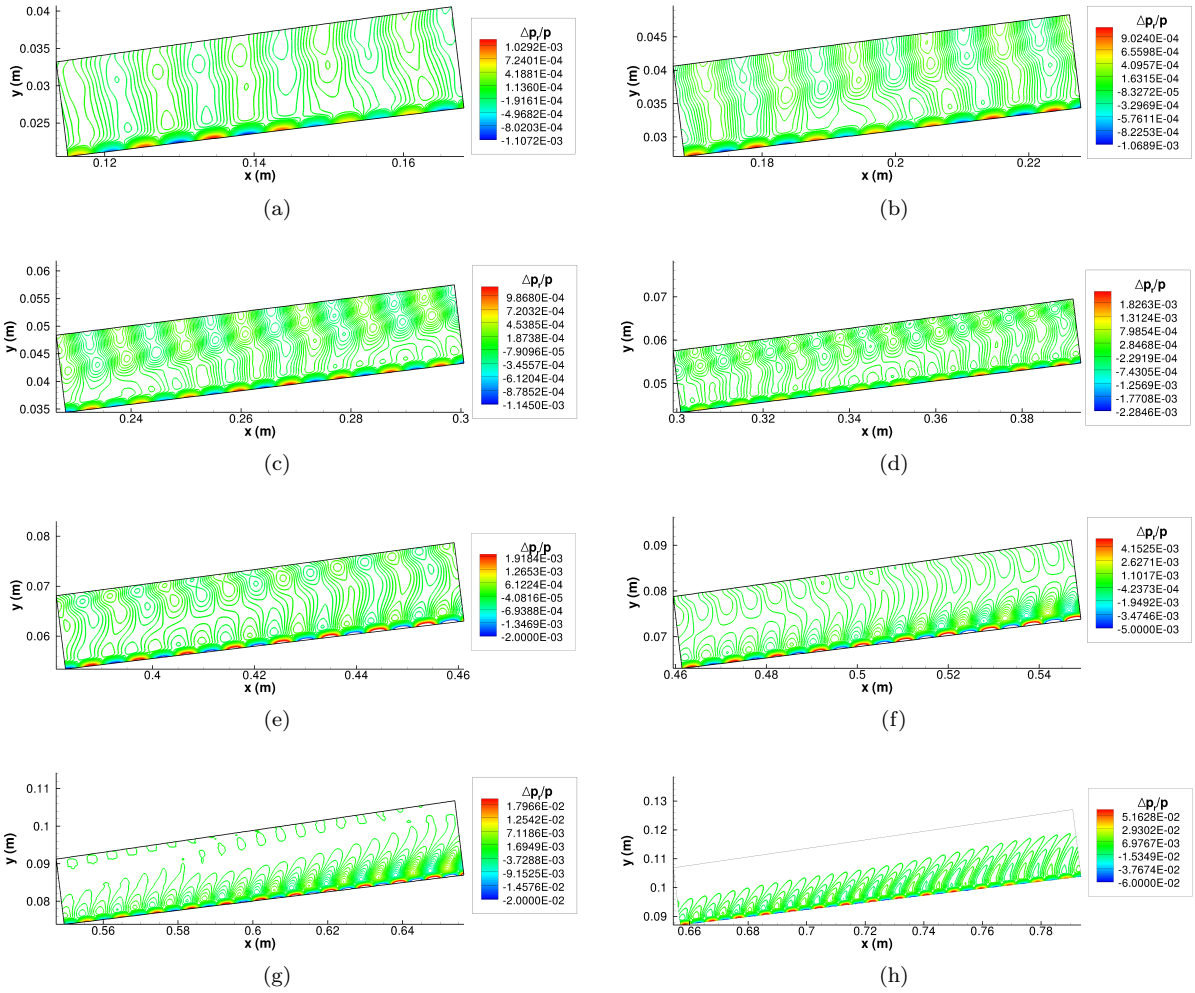

Figure 16. Instantaneous pressure perturbation contour plots for the 525 kHz frequency disturbance.

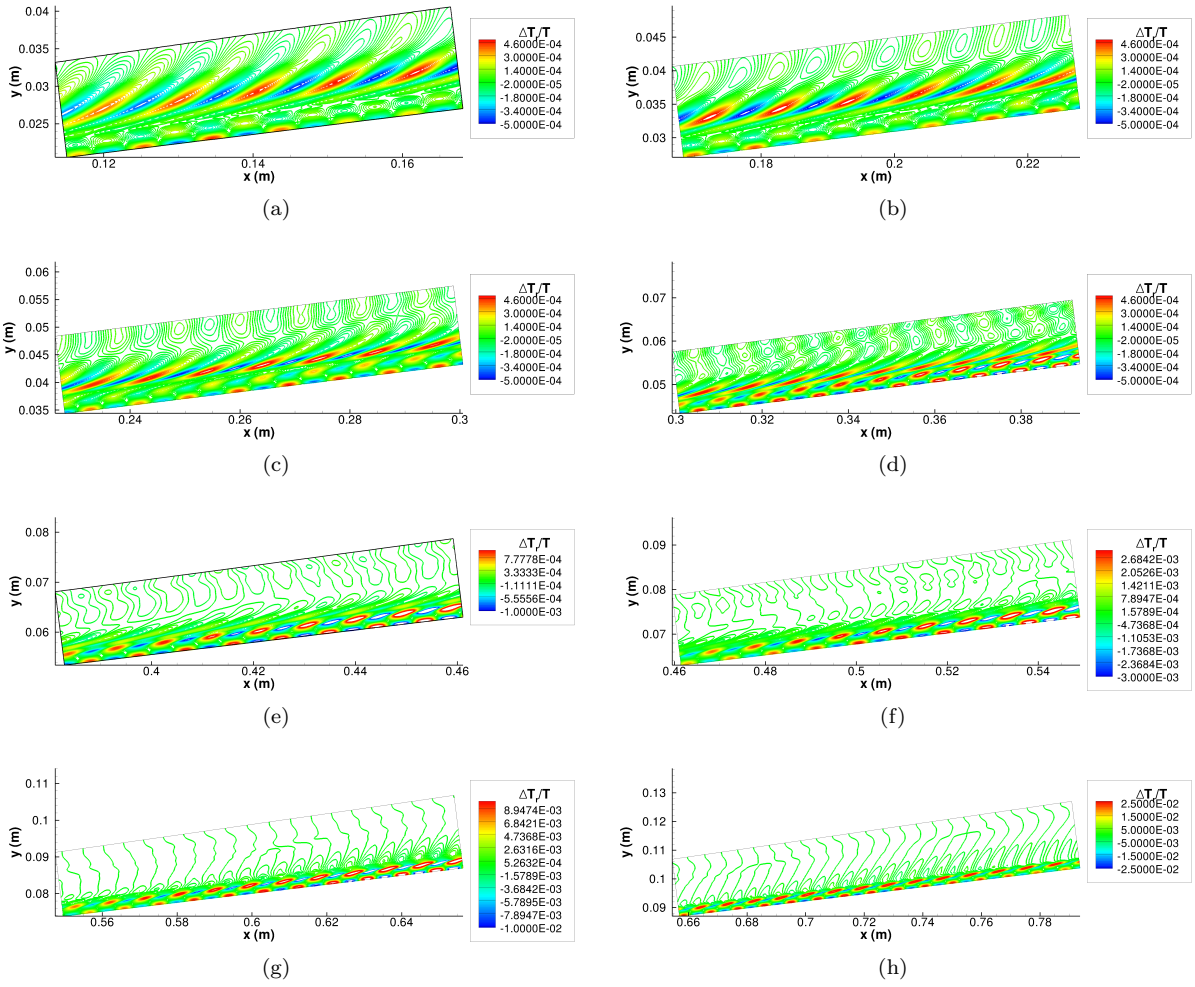

Figure 17. Instantaneous translation-rotation temperature perturbation contour plots for the 525 kHz frequency disturbance.

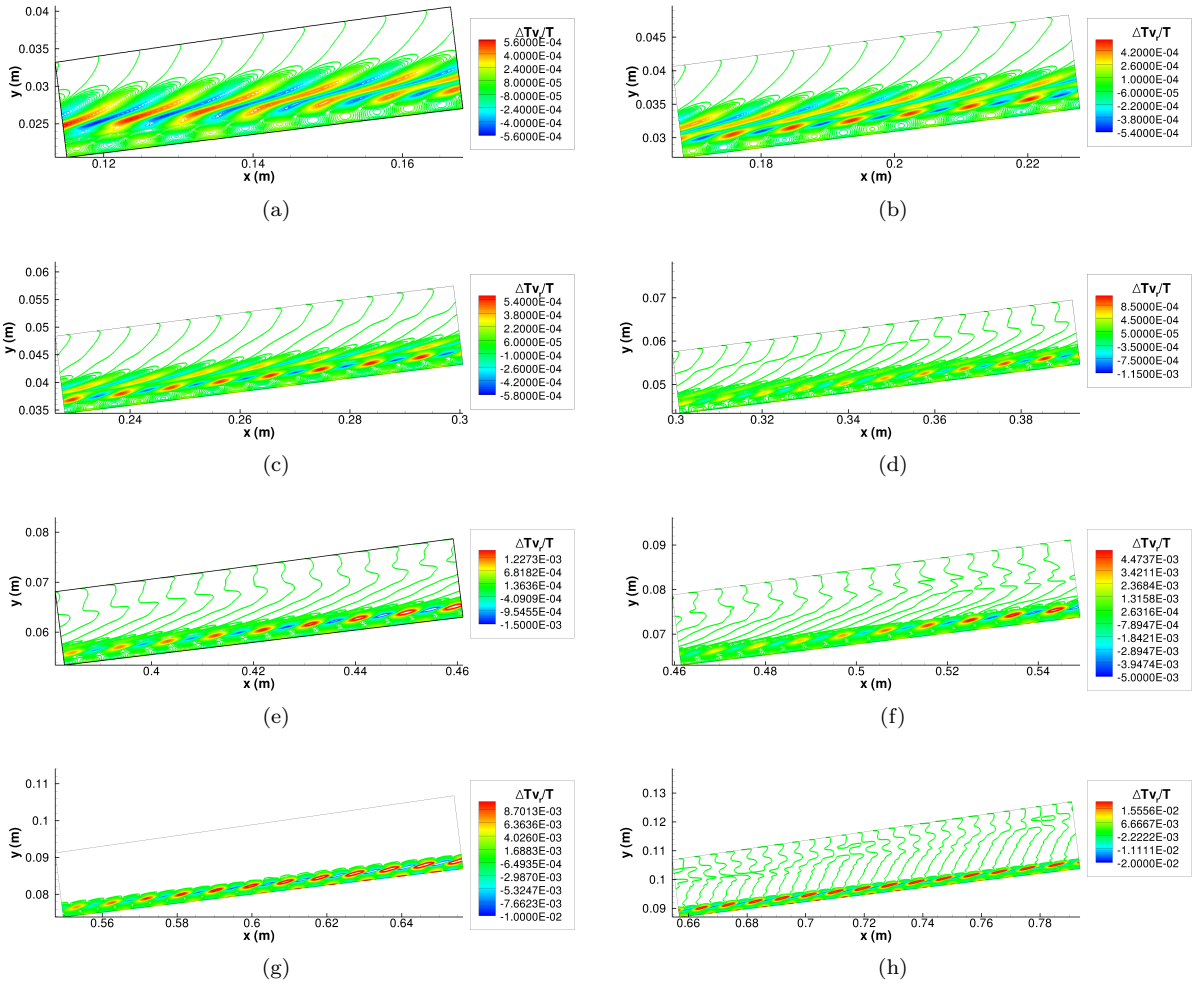

Figure 18. Instantaneous vibration temperature perturbation contour plots for the 525 kHz frequency disturbance.

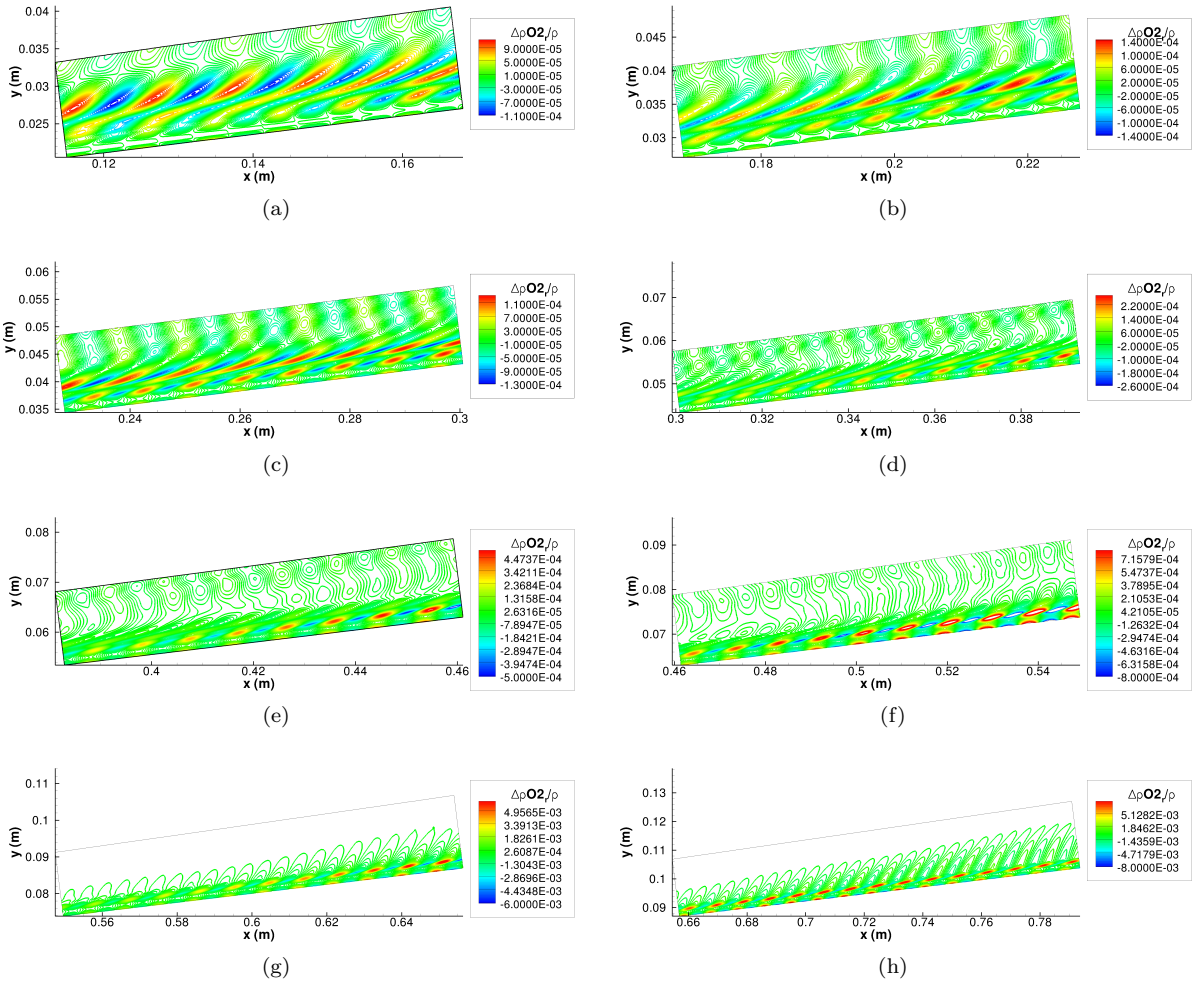

Figure 19. Instantaneous O_2 density perturbation contour plots for the 525 kHz frequency disturbance.

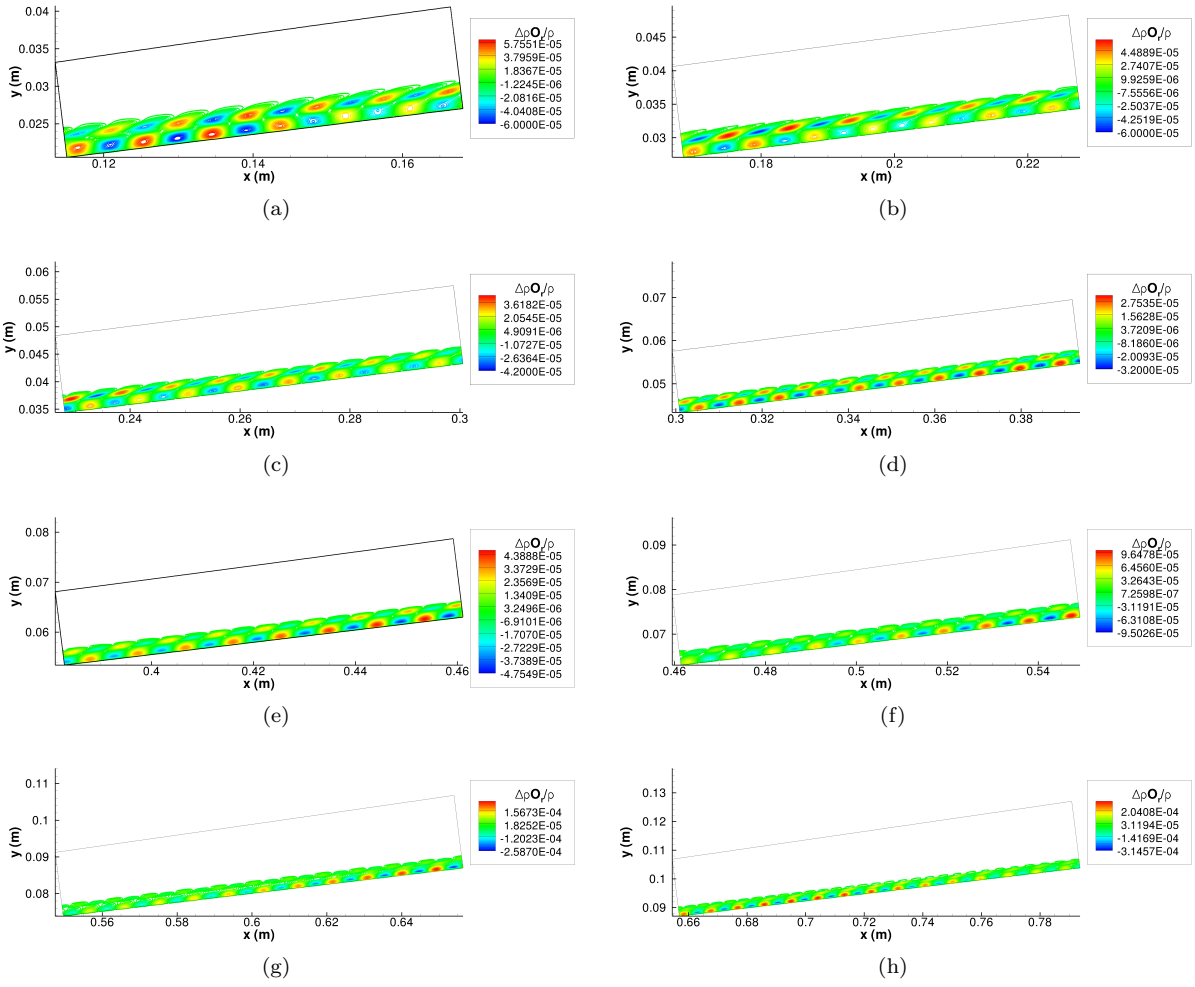

Figure 20. Instantaneous O density perturbation contour plots for the 525 kHz frequency disturbance.